energies

MDPI

Article

A Periodic Horizontal Shell-And-Tube Structure as an Efficient Latent Heat Thermal Energy Storage Unit

Jerzy Wołoszyn * and Krystian Szopa

Faculty of Mechanical Engineering and Robotics, AGH University of Krakow, al. A. Mickiewicz 30, 30-059 Krakow, Poland; kszopa@agh.edu.pl
* Correspondence: jwoloszy@agh.edu.pl

Abstract: Thermal energy storage systems utilising phase change materials offer significantly higher energy densities compared to traditional solutions, and are therefore attracting growing interest in both research and application fields. However, the further development of this technology requires effective methods to enhance thermal efficiency. We propose a horizontal periodic shell-and-tube structure as an efficient latent heat thermal energy storage unit. This research aims to analyse heat transfer not only between the tube containing the heat transfer fluid and the phase change material but also between adjacent shell-and-tube units. The results obtained for a single cell within the periodic structure are compared with those of reference single shell-and-tube units with insulated adiabatic and highly conductive shells. The enthalpy–porosity approach, combined with the Boussinesq approximation, is applied to address the heat transfer challenges encountered during melting and solidification. The periodic horizontal shell-and-tube structure proves to be an efficient latent heat thermal energy storage unit with short melting and solidification times. In contrast, the non-periodic case with neglected conduction in the shell increases the melting and solidification times by 213.8% and 21%, respectively. The shortest melting and solidification times were recorded for the case with a periodic horizontal shell-and-tube structure and shell aspect ratios of 0.44 and 1, respectively.

Keywords: LHTES; CFD; thermal energy storage; phase change material; rectangle shell-and-tube; periodic structure

Citation: Wołoszyn, J.; Szopa, K. A Periodic Horizontal Shell-And-Tube Structure as an Efficient Latent Heat Thermal Energy Storage Unit. *Energies* **2024**, *17*, 5760. https://doi.org/10.3390/en17225760

Academic Editor: Xiaohu Yang

Received: 14 October 2024
Revised: 6 November 2024
Accepted: 14 November 2024
Published: 18 November 2024

1. Introduction

Latent heat thermal energy storage (LHTES) systems using phase change materials (PCMs) are increasingly recognised for their superior efficiency and versatility in thermal energy management. These systems leverage the high latent heat of PCMs to store and release substantial amounts of energy, making them ideal for a wide range of applications. Unlike sensible heat thermal energy storage (SHTES), LHTES can manage large storage volumes while maintaining a stable temperature during the storage process, making it a highly advantageous method [1]. However, the limited thermal conductivity of PCMs often results in reduced heat transfer rates, potentially extending the charging and/or discharging durations within LHTES systems. Researchers and engineers are actively investigating various strategies to improve the thermal efficiency of such systems.

One of the main benefits of LHTES is evident in its integration within concentrated solar power (CSP) plants [2], serving to ensure reliability, enhance efficiency, and bolster economic viability. Another way to effectively use 'solar energy' is by combining LHTES with an Organic Rankine Cycle (ORC) [3], a solar-assisted absorption cooling system [4], or a seasonal space heating system in a single-family building [5]. LHTES systems are employed to control greenhouse temperatures, delivering cooling and heating as needed to meet specific conditions [1]. Furthermore, the LHTES system inside a greenhouse, ideal for summer drying applications, can maintain an optimal drying temperature consistently both day and night [6]. Combining LHTES with a heat pump (HP) allows low-grade energy

storage during peak supply periods, which can then serve as a heat source for the HP during peak demand periods [7]. Zhai et al. [8] showed that compared to the single ground source heat pump (GSHP) heating strategies, integrating the load redistribution heating mode with an LHTES device leads to a 19.1% rise in the average soil temperature recovery rate. Another application of LHTES involves the use of it in single-phase immersion cooling systems to recover waste heat from data centres, thus improving the efficiency of power use [9]. In [10], the authors developed and assessed an efficient snow removal system using a solar thermal energy collector and packed bed LHTES, intending to improve safety for drivers and pedestrians. The utilisation of LHTES is very broad; more information about the applications of such systems can be found in [11].

The construction of LHTES units can vary depending on several factors, including the specific application, available resources, and desired performance characteristics. The PCM can be housed within cavities of various shapes [12], with geometric parameters and relative proportions that significantly influence the behaviour of melting and solidification [13]. A commonly employed technique involves encapsulating PCM within spherical balls, which are then placed in a container alongside a heat transfer fluid (HTF) for efficient thermal transfer [14,15]. This approach can be improved through cascade configurations that incorporate PCMs with varying melting temperatures, ensuring a more uniform process and an increase in the total energy storage [16]. The multi-tube configuration [17] is one of the designs used to enhance the performance of LHTES systems. The optimisation processes for multi-tube constructions [18,19] investigate the most favourable directions within the design variables domain, leading to notable improvements in storage performance. Popular LHTES constructions include shell-and-tube variations such as shell-and-coil-based units [20–22], triplex-tube heat exchangers [23], and other conical, helical, and helical–conical geometries [24]. However, among the shell-and-tube LHTES system constructions, those with straight-axis tubes [25] are arguably still the most commonly encountered solutions, and further studies will focus on these variants.

The low thermal conductivity of PCM is the most significant limitation in applications of the LHTES system. To improve thermal efficiency during melting and solidification processes in shell-and-tube heat exchangers, researchers and engineers implement various heat transfer enhancement techniques [26,27]. The initial widespread strategy involves expanding the surface area for heat transfer by adding fins [28]. The fins can generally be classified as annular [29,30], longitudinal [30,31], spiral [32–34], and discontinuous [35]. The longitudinal fins can adopt various shapes (snowflake [36], tree [37,38], and fractal [39]), often resulting from an optimisation process [40]. The use of metallic fins improves the phase change uniformity and temperature profiles by directing heat towards the dead zones [26]. However, densely packed fins diminish the system's energy density and constrain the exploitation of convection currents [41]. Another approach to enhancing involves increasing the thermal conductivity of PCMs by introducing nanoparticles [42,43], although this method faces challenges in preventing sedimentation. Using porous materials such as metal foams [44] can also improve PCM thermal conductivity, but like fins, it faces a limitation with restricted natural convection flow. Employing multiple PCMs with varying melting temperatures [45,46] can promote uniformity and accelerate the storage process [47]. Additionally, the different shapes of inner tubes [48], their concentric or eccentric positions [49], and the inclination angles of the exchanger [50] may affect the thermal performance of the LHTES unit. Many of the above methods are combined in hybrid solutions [51,52]. Alongside the aforementioned passive heat transfer enhancement techniques, there are active methods that involve mechanical aids, vibration, jet impingement, injection, and external fields. Since active methods are not the focus of this paper, further information can be found in [53].

Circular shells are the most commonly used shape in shell-and-tube designs. This is largely because a circular geometry has the shortest perimeter compared to other shapes. As a result, for an equal volume of PCM, circular cylindrical shells offer the smallest surface area, which helps minimise heat loss to the environment during the melting process [54].

Many studies have analysed the impact of different shell shapes on the thermal performance of thermal energy storage systems. Faghani et al. [55] found that, regardless of the tube shape, a horizontally oriented elliptical shell improves heat absorption and reduces melting time, though it may not be practical for large-scale arrangements. Similarly, Rabienataj Darzi et al. [56] showed that while a vertically oriented elliptical tube reduces melting time, it is less effective during solidification. In a separate study, Khillarkar et al. [57] examined the effects of free convection in a square container, finding that thermal stratification occurs as the heat increases with the convective flow of liquid PCM. Mao et al. [58] investigated how the length-to-diameter ratio affects rectangular containers in shell-and-tube systems, providing design and optimisation recommendations for rectangular LHTES systems. Kumar et al. [54] introduced a semi-circular shell design, which demonstrates a significant enhancement in melting rates, completing the melting of PCM in nearly half the time compared to circular designs. This semi-circular configuration also stores 12% more thermal energy for the same volume of PCM. In a different study, Li et al. [59] focused on a hexagonal shell-and-tube unit, analysing the solidification process and the temperature dynamics using Koch-fractal fins (Wichita, KS, USA). Alizadeh et al. [60] presented a triplex-tube design with hexagonal tubes, while Maneengam et al. [61] examined an octagonal shell-and-tube microsystem, optimising system entropy and irreversibility. However, these studies did not directly compare their findings to circular shell designs. In addition, Shahsavar et al. [62] investigated a vertical double-pipe design featuring a sinusoidal wavy wall, identifying that increasing the wave amplitude and Reynolds number reduced melting and solidification times. The triplex-tube variant with sinusoidal walls was further explored in [63]. Alizadeh et al. [64] optimised a wavy shell unit with curved fins, finding that proper fin geometry enhances thermal penetration towards the outer wall, improving heat transfer rates. Research conducted by Wołoszyn and Szopa [65] revealed that helical-coiled shell structures and spiral fins significantly accelerate PCM melting and solidification processes.

Only a limited number of studies have compared different shell shapes under the same conditions. Qaiser et al. [66] found that elliptical and triangular shells could reduce the PCM melting time by up to 50% compared to circular shells, though solidification was not analysed. Similarly, Hekmat et al. [67] evaluated various shell geometries, including circular, elliptical, square, triangular, and trapezate, in LHTES systems, determining that a downward trapezate shape was most effective for melting, while a horizontal elliptical shape excelled in solidification. Finally, Wołoszyn and Szopa [68] performed an extensive analysis comparing melting and solidification times, liquid fractions, temperature distributions, and heat flux across various shell shapes, including circular, semi-circular, square, rectangular, elliptical, triangular, hexagonal, octagonal, and trapezate, with each shape tested in two orientations. The horizontal rectangular shell exhibited over a 30% reduction in melting time compared to the circular design, achieving the most significant decrease among polygonal shapes. Additionally, the semi-horizontal rectangular and isosceles trapezium shapes in the upward orientation demonstrated high enthalpy during melting, while the upward isosceles trapezium also recorded the shortest solidification time. The research results clearly demonstrate that polygon-shaped shells can be successfully used in shell-and-tube LHTES systems while maintaining or even improving thermal performance, particularly during the melting process.

Another crucial parameter that defines the selected shell is the proportional relationship of its dimensions. Most of the available studies on this topic concern circular shells and describe the shell-to-tube diameter ratio. This applies to shell-and-tube systems in both vertical [69] and horizontal [70] configurations. A review of the studies in this field is presented by Kalapala and Devanuri [71]. The general conclusion that can be drawn from these studies is that the most favourable shell-to-tube diameter ratio is four, taking into account both the melting and solidification processes. Parsa et al. [72] presented studies on the influence of horizontal and vertical obround shells and tube eccentricity on PCM melting. However, the available literature lacks studies describing the impact of shape proportions other than circular ones on thermal performance.

The periodic LHTES system consists of individual shell-and-tube units arranged so that the outer surfaces of the shells are in direct contact with one another. To facilitate efficient heat transfer between the exchangers, the shells should be made from a material with high thermal conductivity. The vast majority of studies describe shell-and-tube systems where the shell is made of a thermally insulating material (usually plexiglas), which is understandable, given the desire to minimise energy loss to the surroundings through the heat exchanger housing. In numerical studies, the most commonly applied boundary condition is an adiabatic wall, which assumes perfect insulation. Studies that used circular shells made of highly conductive material are presented in [73–75]. However, this topic still requires more in-depth investigation, with an extension of the research to periodic and polygon-shaped shells.

Based on an analysis of the existing literature, we identify the research gaps that this study aims to address. To the best of our knowledge, shell-and-tube latent heat thermal energy storage units in a horizontal periodic configuration, as described in the following section, have not been studied to date. Our objective is to conduct an analysis that considers heat transfer not only between the tube containing the heat transfer fluid and the PCM but also between adjacent shell-and-tube units. We propose a horizontal periodic shell-and-tube structure as an efficient latent heat thermal energy storage unit. The results obtained for a single cell within the periodic structure are compared with those from reference single shell-and-tube units featuring insulated adiabatic and highly conductive shells. The shells in periodic structures can have various shapes, including square, rectangular, triangular, trapezoidal, or hexagonal forms. In this paper, we focus on rectangular shapes (including squares) and examine how the aspect ratio of their dimensions, while maintaining a constant mass of PCM, affects heat transfer performance, as well as the melting and solidification times. We also examine the liquid fraction and temperature distribution, heat fluxes on the top and bottom shell edges, and PCM-specific enthalpy changes over time.

2. Research Methodology and Computational Domains

The typical shell-and-tube LHTES unit consists of one or more inner tubes and an outer shell. The heat transfer fluid (HTF) flows inside the tube and exchanges heat with the PCM located between the tube and the shell. In the vast majority of research work, the circular shape of the tube and shell dominates. In our previous research [68], we proved that other shapes, e.g., rectangular, can be effective with additional advantages such as the possibility of arranging into packages (Figure 1). Arranging into periodic packages allows the scale of the solution, but the thermal interaction and behaviour should be addressed.

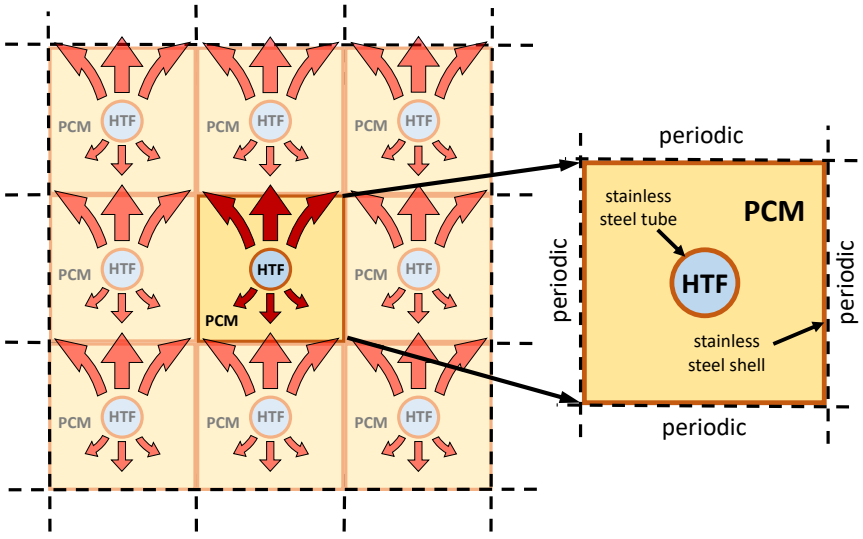

Figure 1. Construction of a periodic rectangular shell-and-tube LHTES with thermal interactions.

This research focuses on the analysis of the periodic horizontal LHTES unit with a rectangular shell shape and is divided into two stages. In the first stage, we perform simulation research to compare a single cell within the periodic structure with those from reference single shell-and-tube units featuring insulated adiabatic and highly conductive shells. We address the influence of the shell design assumptions on the thermal behaviour of LHTES. In Figure 2a, a unit with outer insulation and a low thermal conductivity shell material (e.g., plexiglass) is assumed. In this case, the conduction in the shell can be neglected. In Figure 2b, a unit with good thermal conductivity of the shell is assumed to assess the effect of conduction in the shell, and in Figure 2c, a single LHTES unit is assumed as a periodic structure, taking into account the conduction in the shell material. The dimensions are the same as the aspect ratio in the reference case (AR = 1).

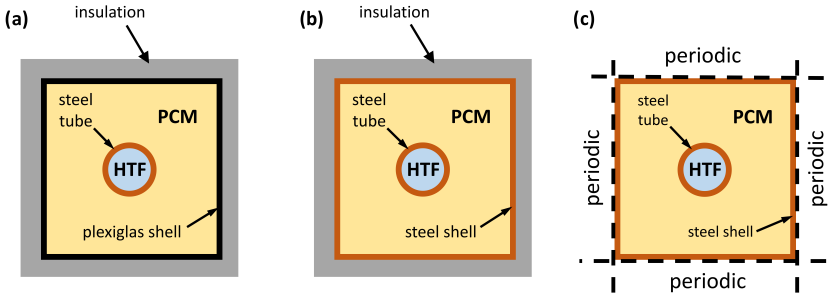

Figure 2. Scheme of compared cases at stage one: (**a**) the unit without shell material and with adiabatic condition on the lateral surface, (**b**) the unit with shell material and adiabatic condition on the lateral surface, (**c**) the single LHTES unit as a periodic structure, taking into account the conduction in the shell material.

The second stage is the analysis of a single LHTES unit as a periodic structure, taking into account the conduction in the shell material and aspect ratios 0.25, 0.33, 0.44, 0.64, 1, 2.26, and 4; see Figure 3.

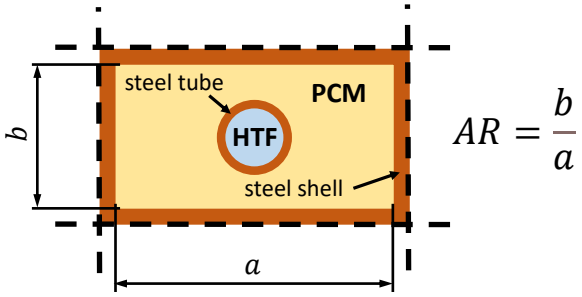

Figure 3. The rectangular single LHTES unit as a periodic structure.

All analyses are prepared assuming the same PCM mass, which guarantees the same stored energy under steady-state conditions and allows for reliable comparison. The characteristic dimensions of the units are presented in Table 1.

Table 1. Geometric parameters of the analysed cases.

Case		AR025	AR033	AR044	AR064	AR1 (Ref.)	AR226	AR4
a	mm	160	140	120	100	80	53	40
b	mm	40	46	53	64	80	120	160
AR	-	0.25	0.33	0.44	0.64	1	2.26	4

The dimensions of the tube are the same for each model: outer diameter d_{to} = 22 mm, and wall thickness w = 1 mm.

We decide to conduct simulation-based research as a fast and accurate technique to compare such LHTES units. Furthermore, employing a 2D domain is chosen as a trade-off to decrease the computational time. The use of numerical models provides a simple comparison of many different constructions to determine the differences and point out the best choice in a short time.

3. Methods and Mathematical Description

Heat transfer in a shell-and-tube energy storage system using a PCM is a complex process governed by the spatial and temporal dynamics of the solid–liquid interface position. This is also a conjugate heat transfer problem that requires sophisticated mathematical models and numerical methods to solve. An additional challenge is the variable nature of the phenomenon, which transitions from conduction in the solid PCM to natural convection in the liquid phase. Solving this complex problem involves the adoption of a series of simplifying assumptions concerning both material and phenomena.

The following assumptions are made:

- The thermophysical properties of the commercially available PCM designated RT54HC (Table 2) are assumed to be independent of temperature and time. The values are adopted from previously published measurement data [68].
- The liquid PCM is an incompressible Newtonian fluid, and the Boussinesq approximation is applied to account for natural convection in the liquid PCM phase. The density is treated as a constant value in all solved equations, except for the buoyancy term in the momentum equation. The buoyancy term is linearised according to Equation (3). The Boussinesq model produces faster convergence compared to the evaluation of fluid density as a non-linear function of temperature.
- A two-dimensional temporal analysis is assumed as a compromise to reduce the computation time.
- The flow of liquid PCM is laminar (Rayleigh number (Ra) is less than 10^8) [76,77]. The Ra ranges from $64 \cdot 10^3$ to $29.1 \cdot 10^6$ depending on the assumed aspect ratio.
- The phase change with the propagation of the solid–liquid interface is utilised by the fixed-grid enthalpy–porosity method [78,79]. This is a common and widely validated method [80–82].
- The volume changes of the PCM during the process are neglected. This assumption is common and allows for a significant simplification of the numerical model without major consequences for the accuracy of the calculations.

The assumed values of the thermophysical properties for the PCM and the stainless steel shell are described in Table 2.

Table 2. Material thermophysical properties (PCM, steel).

Property	Dimension	Value
PCM-RT54HC		
Melting/solidification latent heat	kJ/kg	200/207
Solidus/liquidus temperature for melting	°C	50/60
Solidus/liquidus temperature for solidification	°C	47/53
Specific heat	J/(kg · K)	2100
Thermal conductivity	W/(m · K)	0.2
Dynamic viscosity	Pa · s	0.00365 [83]
The density of solid–liquid	kg/m^3	850/800
Thermal expansion coefficient	1/K	0.000308 [83]
Shell-stainless steel [77]		
Specific heat	J/(kg · K)	502
Thermal conductivity	W/(m · K)	16
Density	kg/m^3	8030

The main justification for choosing RT54HC is the narrow melting/solidification temperature range that ensures that the material can effectively absorb and release heat at a predictable rate. From a practical perspective, a narrow melting/solidification temperature range during the phase change is desirable. It enables efficient thermal energy storage by allowing the heat transfer fluid to operate within a narrow temperature range, providing a clear advantage over water-based storage systems. The RT54HC can store a large amount of thermal energy per unit of mass. This efficiency is especially useful in systems that have limited space but require high thermal management capacity. The RT54HC has excellent thermal stability and can withstand multiple thermal cycles without significant degradation. Many PCMs suffer from phase separation, supercooling, or chemical degradation over time, but the RT54HC resists these issues, ensuring longer operational life and minimal maintenance. The RT54HC exhibits relatively low volume expansion upon melting, so it can be safely enclosed in periodic structure, reducing the risk of structural strain and liquid PCM leakage. Finally, paraffin-based PCM offers a good balance between performance and cost. Compared to other high-performance PCMs that might degrade quickly or require frequent replacement, the RT54HC provides a long-lasting solution, making it more economical for LHTES applications where repeated thermal cycling is common, e.g., in central heating and domestic hot water installations.

3.1. Governing Equations

As a result, it is necessary to solve modified partial differential equations that describe the conservation of mass, momentum, and energy, in accordance with the assumptions outlined above.

The continuity equation for liquid PCM is [77]

$$\nabla \cdot \vec{v} = 0 \tag{1}$$

where v represents the velocity of the fluid.

The momentum equation for liquid PCM is

$$\frac{\partial \vec{v}}{\partial t} + \nabla \cdot (\vec{v}\vec{v}) = \frac{1}{\rho_{ref}}(-\nabla p + \mu \nabla^2 \vec{v} + \rho \vec{g}) + S \tag{2}$$

and

$$\rho = \rho_{ref}(1 - \beta(T - T_{ref})) \tag{3}$$

where $\rho_{ref} = 825$ is the reference density at the reference temperature $T_{ref} = 54.55\,^{\circ}$ C for melting, $T_{ref} = 52.37\,^{\circ}$ C for solidification, and g = 9.81 m/s^2, p denotes the pressure, T represents the temperature, and t stands for the time. The symbol β denotes the expansion coefficient, and μ and S represent the dynamic viscosity and the momentum source term (4), respectively.

The momentum source term S is

$$S = A_{mush}\vec{v}\frac{(1-\alpha)^2}{(\alpha^3 + \epsilon)} \tag{4}$$

where α denotes the liquid fraction, $\epsilon = 0.001$ is a constant value added to prevent division by zero. The mushy zone constant A_{mush} has already been widely discussed [84–86] and varies from 1×10^3 to 1×10^8, so we assume A_{mush} equal to 1×10^5 due to the good agreement with the experimental data.

The thermal energy equation for liquid–solid PCM and shell is

$$\rho_{ref}\frac{\partial H}{\partial t} + \rho_{ref}\nabla \cdot (\vec{v}H) = \nabla \cdot (k\nabla T) \tag{5}$$

where the enthalpy H is

$$H = h_{ref} + \int_{T_{ref}}^{T} c_p dT + \alpha L \tag{6}$$

and the liquid fraction α is

$$\alpha = \begin{cases} 0 & \text{if} \quad T < T_s \\ 1 & \text{if} \quad T > T_l \\ \frac{T-T_s}{T_l-T_s} & \text{if} \quad T_s < T < T_l \end{cases} \tag{7}$$

The proposed mathematical model enables the calculation of the spatial and temporal distributions of the velocity, temperature, and liquid fraction when a moving solid–liquid interface is present.

3.2. Initial and Boundary Conditions

To solve the partial differential equations discussed (Equations (1), (2) and (5)), both the initial and boundary conditions are required. The initial temperature of the entire computational domain and in all cases is $T_{(t=0)} = 30\,^{\circ}\text{C}$ for melting and $T_{(t=0)} = 75\,^{\circ}\text{C}$ for solidification. The initial velocity in the PCM domain is equal to 0 m/s for both melting and solidification.

To simulate heat transfer from HTF to the tube and through the tube, the convective boundary condition is assumed. For HTF such as water, the dynamic viscosity, density, and thermal conductivity vary based on the inlet temperature. Therefore, a different convective coefficient is assumed during the melting and solidification process. The other thermophysical properties of water are maintained at constant values:

$$-k_{htf} \frac{\partial T}{\partial n}|_C = b_{htf,t}(T_{wall} - T_{htf}) \tag{8}$$

where

$$b_{htf,t} = \frac{1}{R_{htf,t} 2\pi r_{to}} \tag{9}$$

To evaluate the heat transfer coefficients between the HTF and the PCM, the thermal resistance is computed. The thermal resistance between the HTF and the outer tube wall is characterised by the heat advection within the tube element and the heat conduction through the tube material (Equation (10)):

$$R_{htf,t} = R_{htf} + R_t \tag{10}$$

Equation (11) below defines thermal resistance due to heat advection within a tube element:

$$R_{htf} = \frac{1}{b_{htf} 2\pi r_{ti}} \tag{11}$$

and

$$b_{htf} = \frac{Nuk_{htf}}{d_{ti}} \tag{12}$$

where the Nusselt number varies based on the flow type and HTF temperature ($T_{htf,m} = 75\,^{\circ}\text{C}$ for melting and $T_{htf,s} = 30\,^{\circ}\text{C}$ for solidification) and is specified using the Petukhov–Gnielinski correlation for turbulent flow ($Re > 2300$) in tubes [76] as shown in (13):

$$Nu = \frac{f/8 \cdot (Re - 1000) \cdot Pr}{1 + 12.7 \cdot \sqrt{f/8} \cdot (Pr^{2/3} - 1)} \tag{13}$$

where

$$f = (0.79 \cdot ln(Re) - 1.64)^{-2} \tag{14}$$

Pr represents the Prandtl number, and the Reynolds number (Re) is determined as follows:

$$Pr = \frac{c_{htf}\mu_{htf}}{k_{htf}}, Re = \frac{\rho_{htf} u d_{ti}}{\mu_{htf}} \quad (15)$$

where c_{htf} = 4180 J/(kg · K), μ_{htf} = 0.0003765 Pa · s, ρ_{htf} = 975 kg/m^3, k_{htf} = 0.665 for $T_{htf,m}$, and μ_{htf} = 0.000797 Pa · s, ρ_{htf} = 995 kg/m^3, k_{htf} = 0.619 for $T_{htf,s}$. The thermal resistance as a result of conduction within the tube material is determined by the following relation (16):

$$R_t = \frac{ln\left(\frac{r_{to}}{r_{ti}}\right)}{2\pi k_t} \quad (16)$$

The HTF mass flow during melting and solidification is assumed to be 4 $\frac{l}{min}$. Based on these data and calculations, the heat transfer coefficients $b_{htf,t}$ (9) are determined to be 1655 $\frac{W}{m^2K}$ and 1152 $\frac{W}{m^2K}$ for the melting and solidification processes, respectively. The walls restricting the flow are subject to the no-slip boundary condition. In the first stage of this investigation and for the AR1a and AR1b cases, the adiabatic boundary condition at the inner and outer shell edges is assumed, respectively. In the AR1a case, the conduction for the shell material (plexiglas shell) is neglected because its thermal conductivity value is close to PCM. In the second stage and for all cases, the periodic boundary condition for opposite sides of the outer shell edge is assumed. In a multi-module LHTES unit, thermal stratification occurs between the top and bottom modules, so the use of periodic boundary conditions represents a compromise between accuracy and computational time. This condition is valid for the middle module and sufficiently enables a comparison of the considered structures. The coupled boundary condition (ideal contact) at the PCM and shell contact surface is assumed (Equations (17) and (18)):

$$-k_{PCM}\frac{\partial T_{pcm}}{\partial n}|_B = -k_{shell}\frac{\partial T_{shell}}{\partial n}|_B \quad (17)$$

$$T_{pcm}|_B = T_{shell}|_B \quad (18)$$

All assumed boundary conditions are presented in Figure 4.

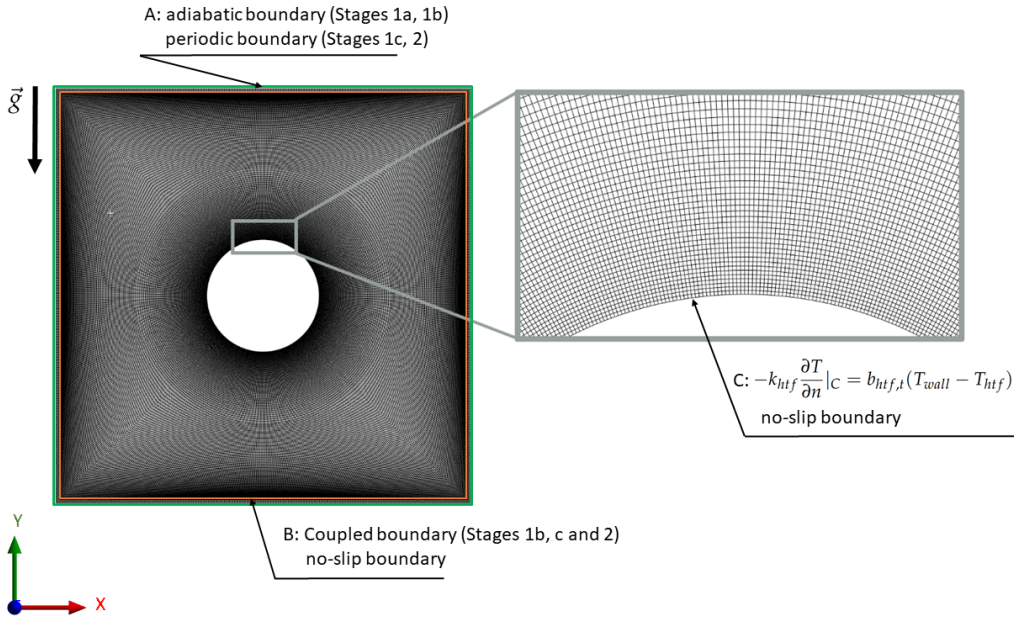

Figure 4. Assumed numerical mesh and boundary conditions for selected case (AR1).

3.3. Numerical Algorithms and Schemes

The numerical calculations are performed with ANSYS Fluent 2021R2 software utilising a pressure-based solver. To couple the continuity and momentum equations, the widely recognised SIMPLE algorithm is used. The PRESTO! scheme is implemented for pressure discretisation, while the Third-Order MUSCL scheme is used for momentum and energy. Gradients are estimated using the Least Squares Cell-Based method due to its computational efficiency compared to the node-based gradient. The convergence thresholds are established at 10^{-5} for the continuity equation, 10^{-6} for the velocity components, and 10^{-8} for the energy equation. For temporal discretisation, a second-order implicit time integration algorithm is used, which is beneficial for its stability. The chosen time step varies according to the cases analysed, ranging from 0.01 to 0.1 s. The maximum number of iterations per time step is equal to 150.

3.4. Verification and Validation

The grid independence test is performed as a verification. The grid consists of quadrilateral control volumes that can provide better accuracy compared to triangular cells, especially for problems involving smooth gradients. A denser grid is employed near the tube and shell boundary (Figure 4) for all cases, ensuring that cell quality remains within acceptable limits. The maximum aspect ratio is 8.82, the maximum skewness is 0.57, and the minimum orthogonal quality is 0.63. All of these least favourable values occur in the AR025/AR4 model. The maximum height of all boundary cells is 0.1 mm, with a growth factor of 1.2 in each case. The maximum size of the control volumes does not exceed 0.5 mm and occurs in regions distant from the tube and the walls of the shell. In Figures 5 and 6, the time-dependent liquid fraction and average PCM temperature values for model AR1 with varying cell counts (ARm1-163200, AR1m2-98560, AR1m3-24960, AR1m4-11840, AR1m5-6360) are shown. During melting, the relative errors in the complete melting time (LF = 1) for AR1m2, AR1m3, AR1m4, and AR1m5 compared to ARm1 are 0.66%, 1.03%, 2.32%, and 4.71%, respectively. The maximum relative errors in average PCM temperature for AR1m2, AR1m3, AR1m4, and AR1m5 compared to ARm1 are 0.45%, 0.7%, 1.5%, and 1.7%, respectively. During solidification, the relative errors in the total solidification time (LF = 0) for AR1m2, AR1m3, AR1m4, and AR1m5 compared to ARm1 are 0.03%, 0.1%, 0.16%, and 0.57%, respectively. The maximum relative errors in the average PCM temperature for AR1m2, AR1m3, AR1m4, and AR1m5 compared to ARm1 are 0%, 0.08%, 0.13%, and 0.34%, respectively. The domain with 98560 cells for model AR1 is adequate for performing the calculations. The maximum value of the time step is selected based on independent studies of the time step [87].

To verify the accuracy of the simulation methodology, the numerical results are compared with the experimental data reported by Kousha et al. [80]. The validation process focuses on a circular shell-and-tube LHTES unit positioned horizontally. Both studies maintain consistency in the geometric and material parameters, along with the boundary and initial conditions. The settings of the fluid dynamics solver are meticulously adjusted according to the details provided in [80]. At the beginning of the melting process, the HTF is set at 80 °C with a flow rate of 0.4 L/min, and a Stefan number of Ste = 0.59 is used in the simulation. Figure 7 illustrates the PCM melting within the shell-and-tube LHTES unit, displaying the average temperature over time. The numerical results show close alignment with the experimental data, with a 5% average error compared to Kousha et al. [80], indicating good correlation during both the preheating and melting stages. Following the complete melting of PCM, the solidification process begins with HTF at 10 °C being introduced into the inner pipe. Figure 7 depicts the average PCM temperature during solidification, showing strong agreement with the experimental results, particularly in the first 2 h. The numerical results for the solidification process deviate by 2.5% on average from the experimental data presented by Kousha et al. [80]. The validation process affirms the robustness of the numerical model, as the results obtained for both the melting and solidification processes are highly consistent with the experimental findings.

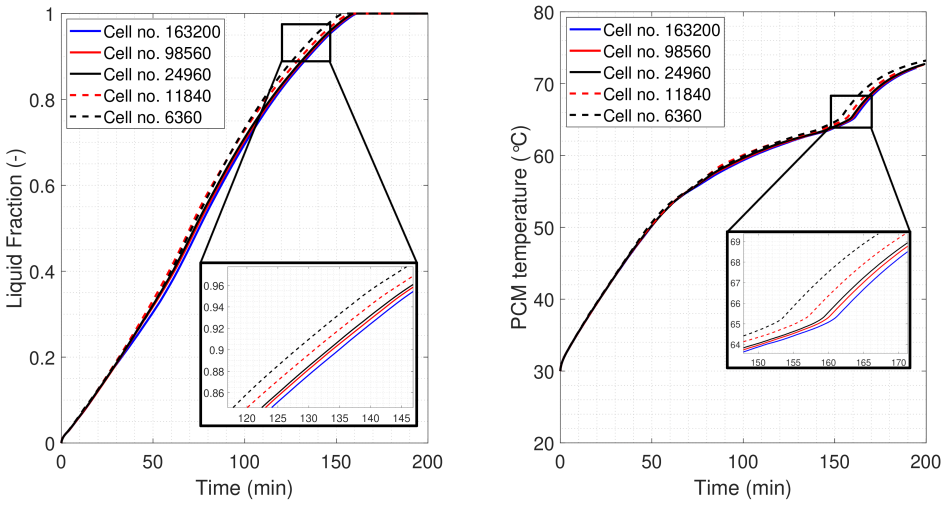

(**a**) (**b**)

Figure 5. Grid independence test for model AR1 during melting: (**a**) liquid fraction, (**b**) PCM temperature.

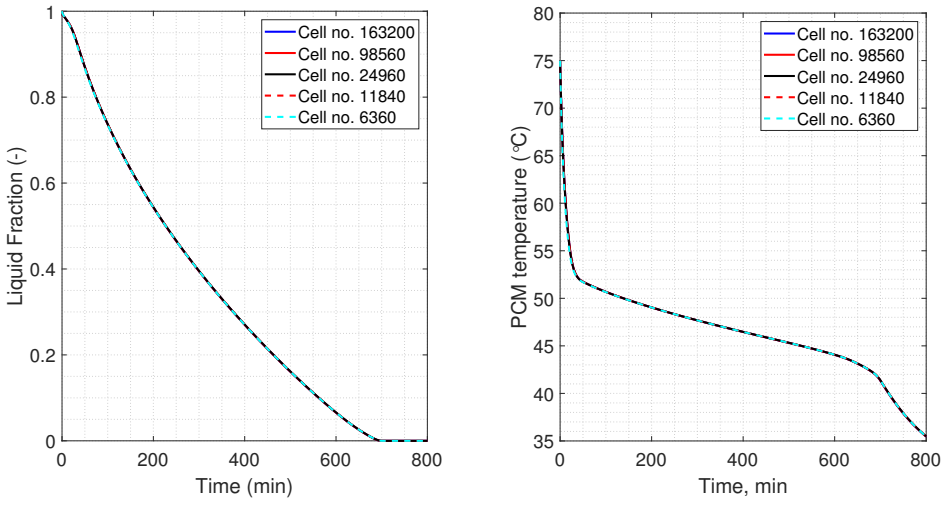

(**a**) (**b**)

Figure 6. Grid independence test for model AR1 during solidification: (**a**) liquid fraction, (**b**) PCM temperature.

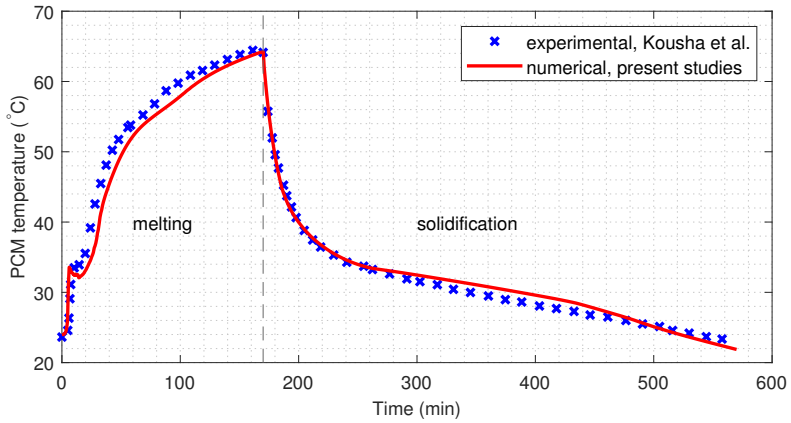

Figure 7. Validation of the numerical model by comparing the average PCM temperature during the melting and solidification process with experimental results presented by Kousha et al. [80].

4. Calculation Results and Discussion

The results of the simulations for both the melting and solidification processes are examined individually to evaluate the effects of different scenarios on the performance of the LHTES, independent of the prior phases. This method enables the identification of configurations that favour either melting or solidification. In several practical scenarios, achieving a balance between the melting and solidification times is crucial. Nevertheless, this relationship is highly specific to the application in question. Within the scope of this study, it is important to note that the melting time is primarily emphasised when comparing individual LHTES units. This focus is critical in situations requiring high power absorption during brief peak sunshine periods, like those from solar collectors. Furthermore, in many applications, such as heating systems, the discharge duration is less significant due to the typically continuous nature of energy demand. As part of the research discussion, the phase change times, both overall (Tables 3 and 4) and for various liquid fraction stages (Figures 8 and 9), the temperature and liquid fraction distributions are analysed and compared. Additionally, area-weighted averages of the PCM domain temperature, liquid fraction, specific enthalpy, and heat flux values over time for the top and bottom edges are calculated and recorded at 1-s intervals.

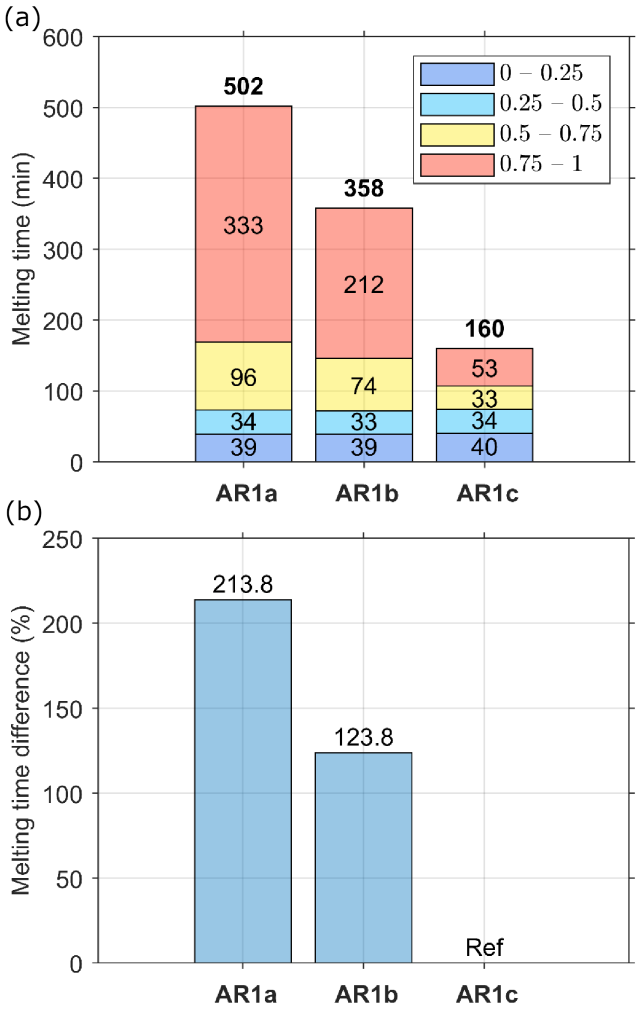

Figure 8. Melting process for cases presented in Figure 2, (**a**) timestamps for liquid fraction values of $\alpha = \{0.25,\ 0.5,\ 0.75,\ 1\}$, and (**b**) percentage difference in melting time compared to the reference case AR1c.

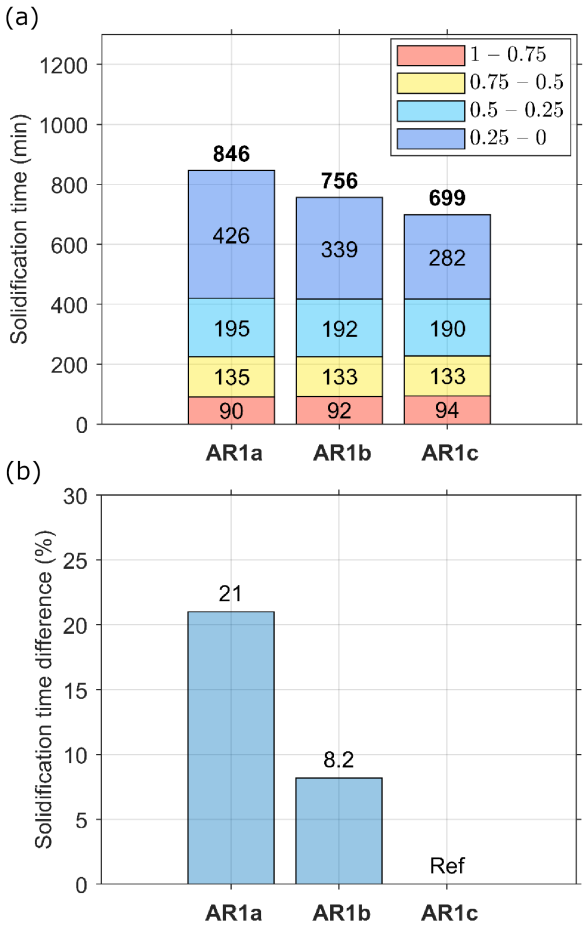

Figure 9. Solidification process for cases presented in Figure 2, (**a**) timestamps for liquid fraction values of $\alpha = \{0.75,\ 0.5,\ 0.25,\ 0\}$, and (**b**) percentage difference in solidification time compared to the reference case AR1c.

Table 3. The average PCM temperatures, specific enthalpy change, and time required to reach a liquid fraction of $\alpha = 1$ during melting and $\alpha = 0$ during solidification, for cases presented in Figure 2.

Model	Melting			Solidification		
	Time for $\alpha = 1$	$T_{PCM,avg}$	$h_{PCM,m}$ for t = 160 min	Time for $\alpha = 0$	$T_{PCM,avg}$	$h_{PCM,s}$ for t = 699 min
	min	°C	kJ/kg	min	°C	kJ/kg
AR1a	502	71.12	223.48	846	35.68	262.13
AR1b	358	70.75	231.16	756	38.74	264.53
AR1c	160	65.43	274.42	699	41.39	267.09

Table 4. The average PCM temperatures, specific enthalpy change, and time required to reach a liquid fraction of $\alpha = 1$ during melting and $\alpha = 0$ during solidification, for periodic LHTES units with various aspect ratios.

Model	Melting			Solidification		
	Time for $\alpha = 1$	$T_{PCM,avg}$	$h_{PCM,m}$ for t = 143 min	Time for $\alpha = 0$	$T_{PCM,avg}$	$h_{PCM,s}$ for t = 699 min
	min	°C	kJ/kg	min	°C	kJ/kg
AR025	150	63.66	261.52	928	39.96	240.07
AR033	145	64.00	268.39	865	40.10	246.73
AR044	143	64.40	272.32	786	40.29	256.42
AR064	148	64.79	268.50	732	40.84	263.01
AR1	160	65.40	258.09	699	41.39	267.09
AR266	199	66.17	233.47	807	40.26	253.15
AR4	244	66.59	213.07	958	39.62	236.00

4.1. Influence of the Shell Design Assumptions on LHTES Behaviour

In the first stage, we analyse and compare horizontal shell-and-tube LHTES units, and the main emphasis is placed on comparing cases with different approaches to the shell edge treatment. Case AR1a is the unit with neglected conduction in the shell material due to low thermal conductivity. Case AR1b is the single unit with conduction in the shell material and insulated outer shell edge. The AR1c case is the periodic unit with conduction in the shell material. In Table 3, we compare the times required to reach a liquid fraction of $\alpha = 1$ during melting and $\alpha = 0$ during solidification (cases AR1a–AR1c), the average PCM temperatures, and the specific enthalpy. The PCM specific enthalpy change is read for the shortest melting (t = 160 min) and solidification (t = 699 min) times.

The use of a highly conductive shell (case AR1b) reduces the melting (28.7%) and solidification (10.6%) times compared to AR1a (case without the conductive shell). However, the shortest melting time and the highest enthalpy change are observed for the periodic unit with a highly conductive shell (case AR1c) (Table 3). This improvement is mainly due to heat conduction in the shell material but, more significantly, also to the periodic structure of the unit, which causes the bottom of the unit to be heated by the module below. As a result, the average PCM temperature in the unit (A1c) is lower than in other cases (A1a,b) when the entire PCM has melted (Table 3). However, in this case (A1c), almost all storable energy becomes available in a short time (the highest specific enthalpy is achieved in the shortest time). Considering the well-conducting walls (A1b) of the shell leads to a higher PCM temperature near the lower corners of the shell, which accelerates the melting process. Neglecting conduction in the shell increases the melting and solidification times of the PCM by 213.8% and 21%, respectively. For the configuration that accounts for conduction (AR1b) but without periodic condition, the melting and solidification times are 123.8% and 8.2% longer, respectively (Figures 8a and 9b).

In Figures 8a and 9a, we compare the melting and solidification times for four stages, representing different ranges of the liquid fraction: 0 to 0.25, 0.25 to 0.5, 0.5 to 0.75, and 0.75 to 1. The first two stages (liquid fraction up to 50%) of both the melting and solidification processes between the analysed cases have similar times. The first stage is 39–40 min, the second stage 33–34 min, then 90–94 min, and 133–135 min for melting and solidification, respectively. This uniformity arises because the melting and solidification phenomena occur at the same surface area and under identical conditions. This is also confirmed by the almost identical change in the liquid fraction up to 80 min (Figure 10) and up to 400 min (Figure 11). The largest differences between the analysed cases are seen in the final two stages (0.5 to 0.75 and 0.75 to 1), especially for the melting phenomenon, where AR1a has a significantly longer melting time compared to AR1b and AR1c. The AR1c case consistently has the shortest melting and solidification times in stages three and four, making it the most efficient configuration in terms of melting and solidification times. In the melting period, the bottom part of the AR1c is continuously heated, and convective heat transfer is present. This is visible in the liquid fraction and temperature distribution in Figures 10 and 12. In the AR1b case, additional heating occurs only through the lateral surfaces, slightly increasing the temperature in the lower part of the PCM, but conduction remains the dominant heat transfer mechanism. In the AR1a case, conduction dominates, especially below the tube, where the heat transfer intensity is much lower than that of convection. During the solidification period, the top part of the AR1c is continuously cooled down by the bottom of the upper unit and the additional heat transfer occurring. The consequence is a higher average PCM temperature (from 400 to 740 min) than for cases AR1a and AR1b (Figure 13). The advantage of the AR1c case is a lower PCM temperature in the upper part of the unit, which consequently accelerates the process compared to the AR1a and AR1b cases. This is visible in liquid fraction and temperature distribution in Figures 11 and 13.

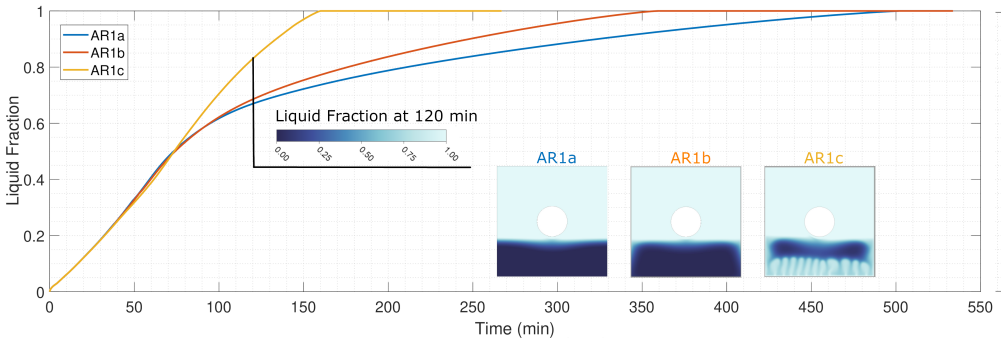

Figure 10. Average PCM liquid fraction over time during melting for cases presented in Figure 2.

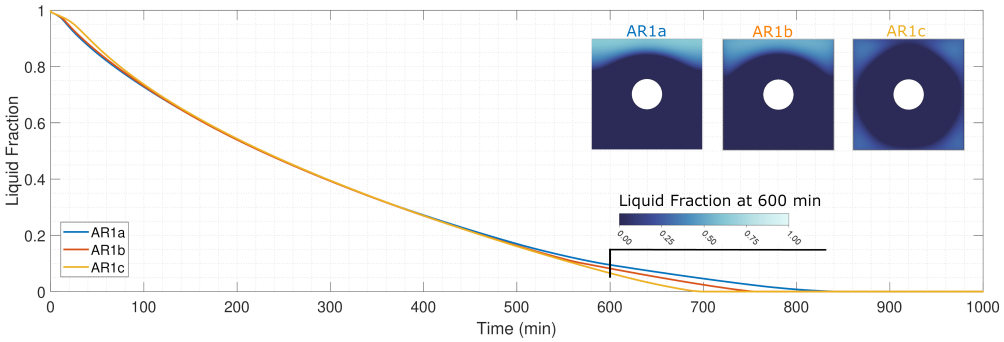

Figure 11. Average PCM liquid fraction over time during solidification for cases presented in Figure 2.

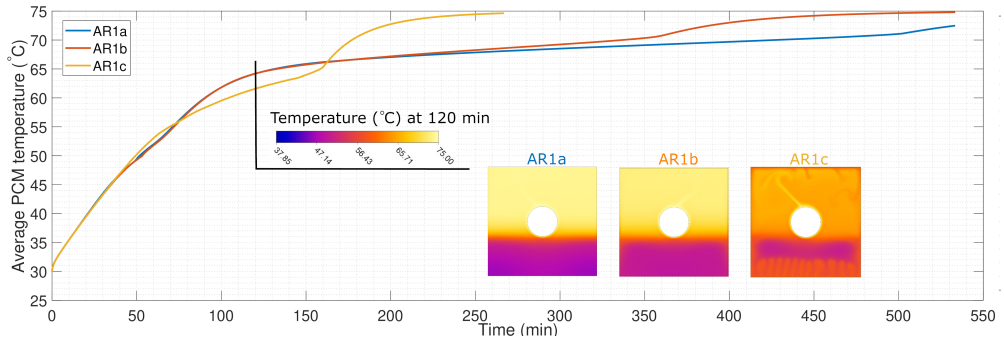

Figure 12. Average PCM temperature over time during melting for cases presented in Figure 2.

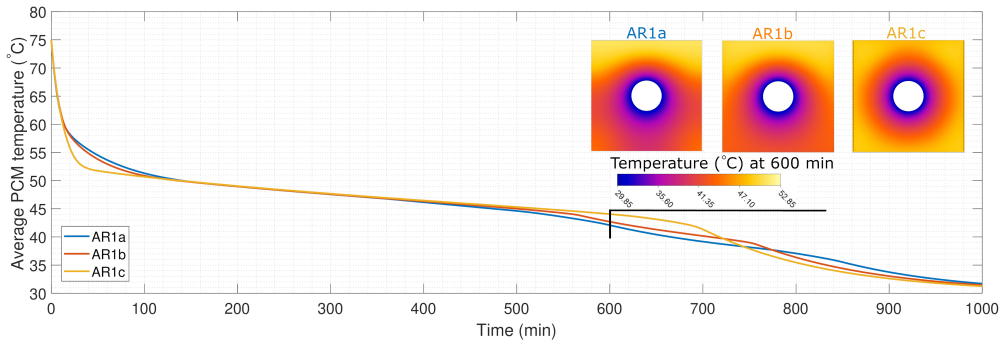

Figure 13. Average PCM temperature over time during solidification for cases presented in Figure 2.

Figures 14 and 15 present the average heat flux values over time for the top (a) and bottom (b) edges during the melting and solidification processes. Negative values indicate heat being transported out of the PCM domain, while positive values indicate that heat is supplied to the PCM. In the AR1a case, the heat flux is 0 W/m^2 due to the assumed

adiabatic condition on the lateral edge and neglected shell material (low shell thermal conductivity). In the AR1b case, during both processes, a small value of heat flux to or from the shell is noticeable, which is mainly due to conduction in the shell material and the adiabatic condition at the outer edge of the shell. In the AR1c case during the melting process, a noticeable increase in the absolute heat flux value for the top edge is observed from around the 10th minute (Figure 14a). This sharp increase, followed by subsequent flattening, indicates that the AR1c configuration allows for rapid heat transfer initially, with significant energy release to the upper unit, suggesting a faster melting process for the entire LHTES unit. After 160 min, the absolute heat flux value decreases to 0 W/m^2, indicating that the phase change is complete. At the bottom edge of the unit (Figure 14b), an analogous situation is observed; this time, energy is intensively supplied to the lower part of the PCM, which consequently accelerates the overall melting process. A similar situation but with less intensity is seen for the solidification process. There is a rapid heat flux increase from the very beginning, which indicates intense heat transfer from the upper PCM part to the top edge and consequently to the lower part of the next unit (Figure 15a,b). This consequently causes faster cooling of the liquid PCM than in other cases and the fastest phase change in the solidification process.

Figures 16 and 17 show the change in PCM specific enthalpy compared to the maximum possible specific enthalpy (h_{max}) during melting and solidification.

The specific enthalpy change in the PCM domain is calculated as average values over the domain, and the maximum enthalpy during melting and solidification processes is calculated according to Equation (19):

$$h_{M|S,\max} = c_{PCM}|T_{wall} - T_{ini}| + L_{M|S} \quad (19)$$

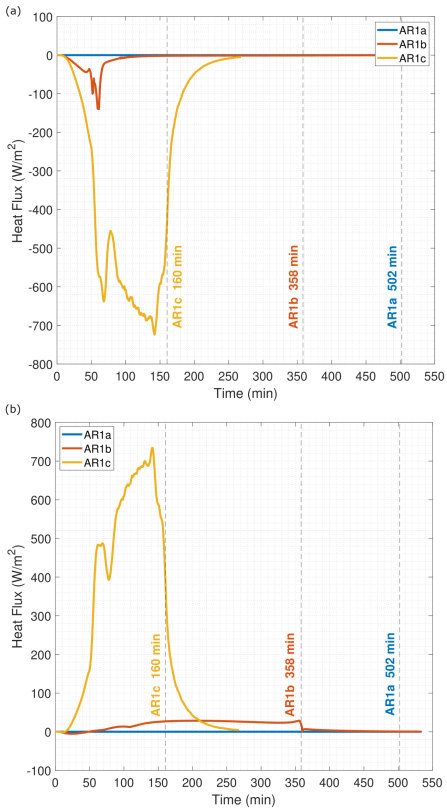

Figure 14. Heat flux average values for the top (**a**) and bottom (**b**) edges during melting for the cases presented in Figure 2.

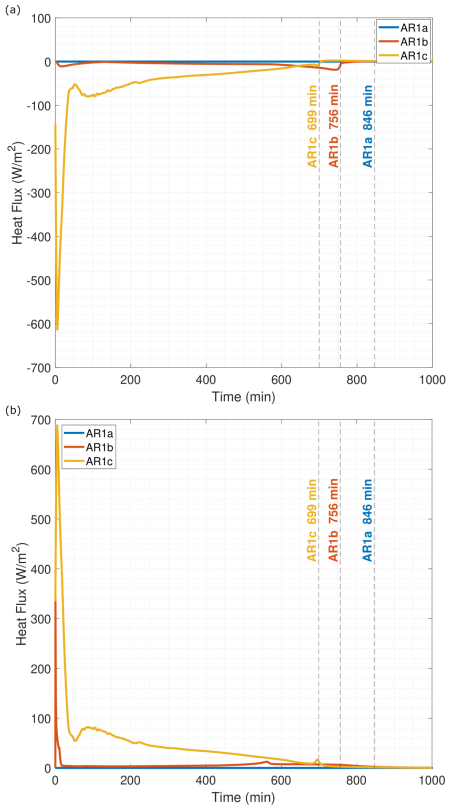

Figure 15. Heat flux average values for the top (**a**) and bottom (**b**) edges during solidification for the cases presented in Figure 2.

The highest specific enthalpy change during melting, occurring in the shortest time, is achieved in the AR1c case (160 min). The enthalpy change increases most slowly in the AR1a case. These observations clearly correlate with changes in the average PCM temperature and the liquid fraction over time. All three cases (AR1a, AR1b, and AR1c) exhibit a steep increase in specific enthalpy (up to 100 min), indicating that the PCM rapidly absorbs heat and transitions from solid to liquid, regardless of the conditions at the shell. This behaviour is characteristic of the initial phase of the melting process. The highest specific enthalpy change during solidification, occurring in the shortest time, is achieved in the AR1c case (699 min). All three cases (AR1a, AR1b, and AR1c) show the same enthalpy decrease up to the 650th min. This indicates that the presence of a conducting shell or a periodic structure has no significant influence on the nature of the enthalpy changes.

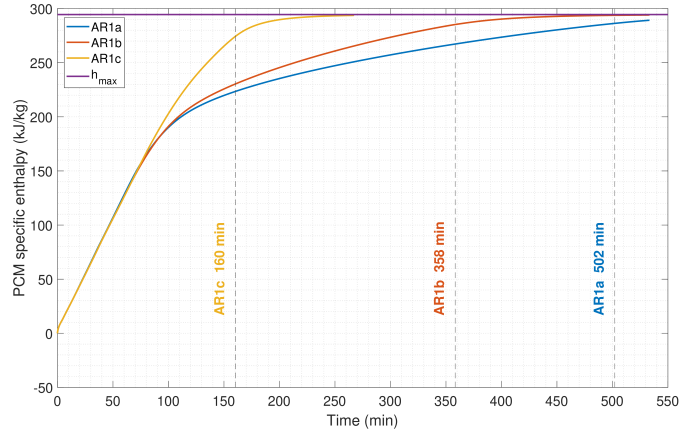

Figure 16. Specific enthalpy over time during melting for cases presented in Figure 2.

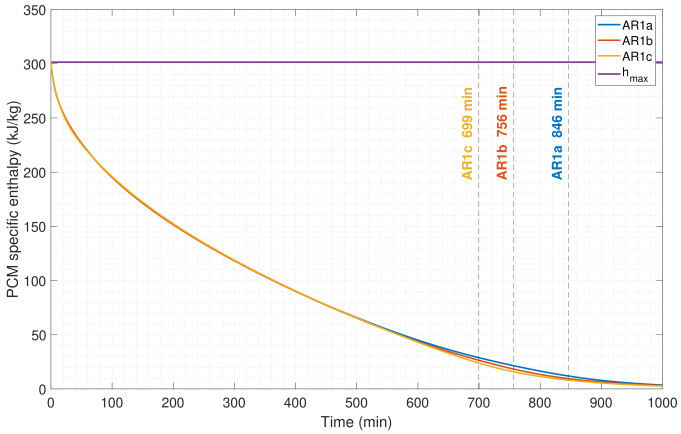

Figure 17. Specific enthalpy over time during solidification for cases presented in Figure 2.

4.2. Influence of Rectangular Shell Aspect Ratio

In the second stage, we analyse a single rectangular horizontal shell-and-tube LHTES units as a fragment of a larger periodic structure. The main emphasis is placed on the impact of the shell aspect ratio on the LHTES thermal performance. In Table 4, we compare the melting and solidification times, as well as the average PCM temperature, when the liquid fraction reaches $\alpha = 1$, $\alpha = 0$, respectively. The PCM specific enthalpy change is read for the shortest melting (t = 143 min) and solidification (t = 699 min) times. The shortest melting time is achieved for an LHTES shell with an aspect ratio of 0.44 (AR044-143 min), and the shortest solidification time is achieved for an LHTES shell with an aspect ratio of 1 (AR1-699 min). Firstly, this is the result of the distance from the tube to the bottom edge being smaller than in the reference case (AR1), which enhances heat transfer in the lower part of the LHTES unit due to decreased thermal resistance. Secondly, in the horizontal direction, the distance from the pipe to the lateral surface is smaller than in AR025 and AR033, which also results in lower thermal resistance. The longest times in the melting and solidification processes are for AR4 (244 min, 958 min). This is because, during the melting process, a thick layer of solid PCM exists below the pipe, providing significant thermal resistance to the energy supplied from the bottom edge and the pipe. Conduction remains the dominant heat transfer mechanism. In the case of solidification, conduction also dominates. The thickness of the liquid PCM layer in the vertical direction is much greater than in the reference case, which means that the thermal resistance will also be greater. The temperatures at which PCM fully melts are fairly similar in all cases, ranging from 63.66 °C (AR025) to 66.59 °C (AR4), showing that the aspect ratio has little impact on the average PCM temperature during melting. Similar findings hold for the solidification process. It can be observed that cases with a low shell aspect ratio (horizontal–AR033, AR044, AR064) allow for storing large amounts of energy in a short time (specific enthalpy change: 268, 272, 268 kJ/kg). The cases with a large aspect ratio (vertical AR266, AR4) are characterised by a lower enthalpy value and therefore lower stored energy than the fastest case (AR044).

Figures 18 and 19 present the melting and solidification times at four different stages, along with the relative time differences compared to the AR1 reference case. The first stage (liquid fraction up to 25% or 75%) of both the melting and solidification processes across the analysed cases have similar times, 38–43 min and 91–108 min for melting and solidification, respectively. These small differences during melting/solidification are due to the same tube surface area and identical boundary conditions. Therefore, the dynamics of the first stage of the both melting and solidification stages are independent of the shell aspect ratio. The melting time for AR025, AR033, AR044, and AR1 in each stage is more evenly distributed compared to cases with higher aspect ratios (AR226, AR4). This means that compared to the cases with a high aspect ratio, the process is more uniform. The long melting time (AR226 and AR4) in the fourth stage is due to the lower heat transfer intensity than in the

other cases. As was mentioned earlier, conduction dominates in the lower part of the unit. Negative percentage values for AR025 (−6.3%), AR033 (−9.4%), AR044 (−10.6%), and AR064 (−7.5%) indicate that these configurations melt faster than the reference case (AR1). AR044, in particular, melts 10.6% faster than AR1. The positive percentage values AR226 (24.4%) and AR4 (52.5%) show a significant increase in melting time. AR4, in particular, takes 52.5% longer to melt compared to the reference case, making it the least efficient design for melting among the models. In the solidification process, all analysed cases have longer solidification times than the reference case (AR1). For AR025 and AR4, the times are 32.8% and 37.1% greater than the reference case, respectively. This is due to the larger distances between the heat source and the shell wall in these configurations, which result in higher thermal resistance and slowdown of the entire process.

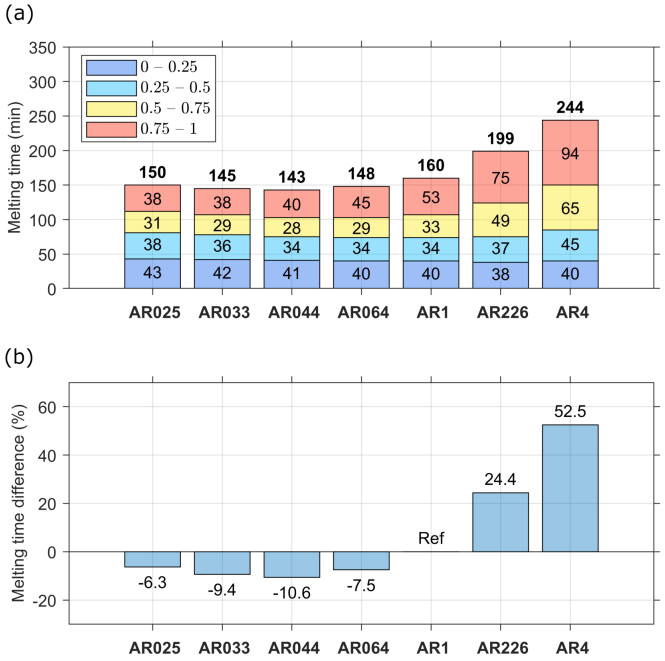

Figure 18. Melting process for periodic LHTES units with various aspect ratios (**a**) timestamps for liquid fraction values of $\alpha = \{0.25,\ 0.5,\ 0.75,\ 1\}$, and (**b**) percentage difference in melting time compared to the reference square shape AR1.

In Figures 20 and 21, we compare the liquid fraction over time and its spatial distribution at 115 min for the melting process and 320 min for the solidification process. The beginning of the melting process (up to 75 min) is similar and occurs with the same dynamics in all compared cases. This is related to the evolution of the liquid phase near the heat source, which does not depend on the shape of the shell. After about 100 min, in the high-aspect-ratio cases (AR226, AR4), a slowdown of the melting process is visible due to the passage of the liquid PCM below the heat source and, consequently, the dominance of conduction for these cases. In the liquid fraction distributions, we can observe that for cases AR226 and AR4, convective currents are just beginning to form, which is significantly delayed compared to the fastest case (AR044). However, in the case of AR025, despite the rapid phase change occurring above and below the tube, we also have clear areas of solid PCM in regions farthest from the heat source, which is not obvious. In each case, the influence of the lower unit is visible, resulting in the creation of convection currents that form at the lower edge of the shell. However, the width of this lower edge in the periodic configuration is not unlimited. In the solidification process due to conduction dominance, the case with the smallest distance from the tube to the shell corner is beneficial (AR1). Increasing or decreasing the aspect ratio in this case extends the phase change time. The

periodic structure and low aspect ratio cases allow for a faster temperature reduction at the top of the unit but ultimately do not accelerate the entire process.

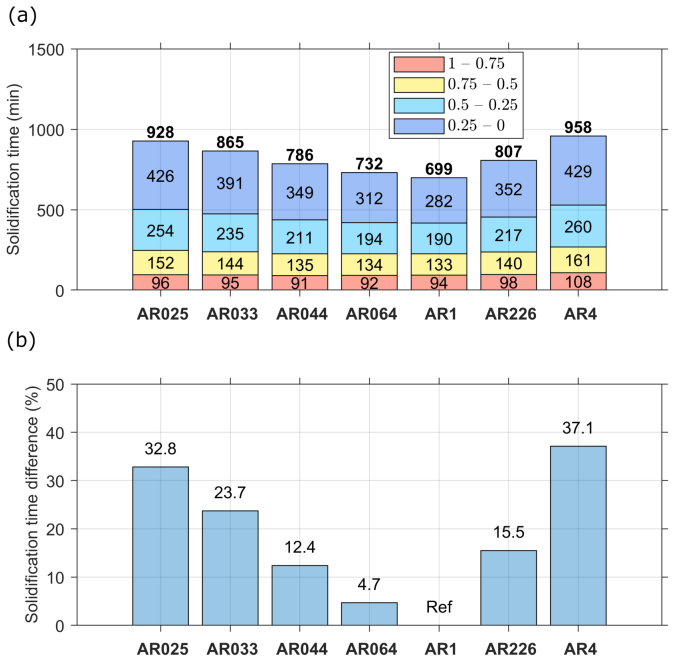

Figure 19. Solidification process for periodic LHTES units with various aspect ratios (**a**) timestamps for liquid fraction values of $\alpha = \{0.75,\ 0.5,\ 0.25,\ 0\}$, and (**b**) percentage difference in solidification time compared to the reference square shape AR1.

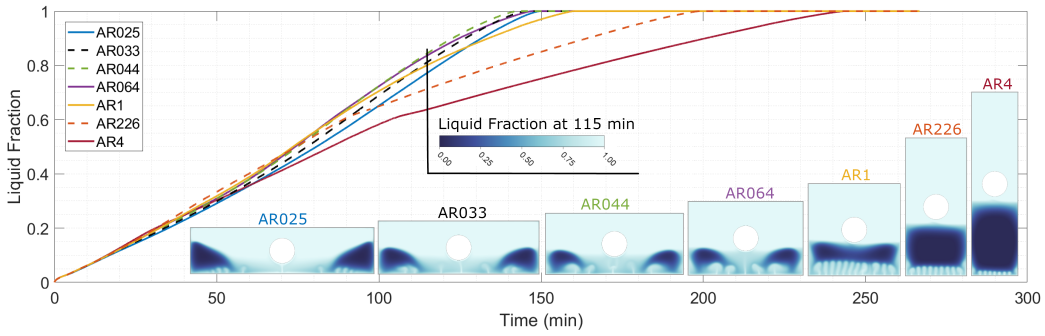

Figure 20. Average PCM liquid fraction over time during melting for periodic LHTES units with various aspect ratios and LF spatial distribution at 115 min.

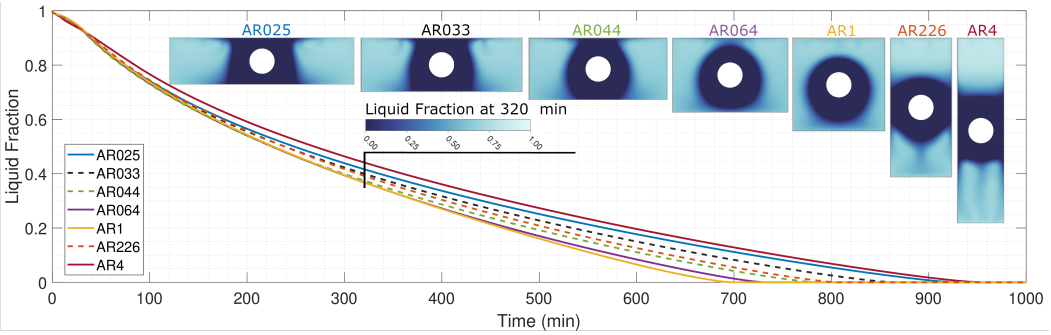

Figure 21. Average PCM liquid fraction over time during solidification for periodic LHTES units with various aspect ratios and LF spatial distribution at 320 min.

In Figures 22 and 23, we compare the PCM average temperature over time and its spatial distribution at 115 min for the melting process and 320 min for the solidification process. Similarly to the liquid fraction, the dynamics of the average PCM temperature increase in the initial stage of the melting process are the same in each case considered. A slight acceleration in the increase in the average PCM temperature can be observed for the AR226 and AR4 configurations at 90 min and 110 min, respectively. This is the result of the phase change interface passage below the tube and a gradual increase in the liquid PCM temperature above the pipe. The dynamics of changes consistently decrease due to the significant area with a temperature below the phase change temperature. In the period 140–160 min, there is a significant increase in the average PCM temperature value for the remaining configurations. This is the end of the melting process, and a liquid PCM is heated up to heat source temperature. A characteristic feature of the shell-and-tube periodic structure unit is the presence of additional convection currents at the bottom and top edges. In Figure 22, the temperature distribution with visible convection currents of hot and cold liquid PCM is presented. The low aspect ratio, and therefore wide shells are characterised by a larger heat transfer surface. However, since the main heat source is the tube, in a low aspect ratio configuration, there are relatively large areas of solid PCM (e.g., AR025 vs. AR044). This is a consequence of the higher distance from the heat source and the thermal resistance. At the beginning of the solidification process (up to 40 min), we observe a rapid decrease in the average PCM temperature in all analysed cases. As the temperature approaches the phase change point, the process slows down significantly, which is characteristic of PCMs. After 700 min, the phase change is complete for each configuration, and a further, faster temperature decrease occurs until the temperature of the heat source is reached. Since convection quickly gives way to conduction during solidification, the configuration with an aspect ratio of one is the most favourable. This is due to its lowest thermal resistance. Regardless of whether we are dealing with a case with the largest or smallest aspect ratio, the AR025 and AR4 configurations exhibit almost identical changes in the average PCM temperature.

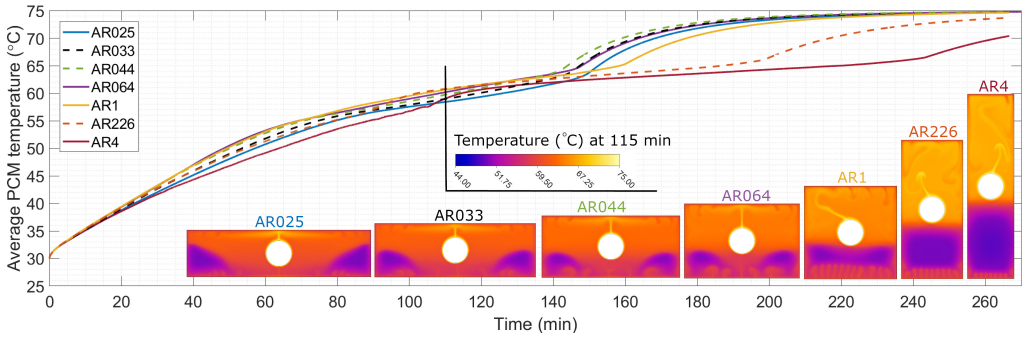

Figure 22. Average PCM temperature over time during melting for periodic LHTES units with various aspect ratios.

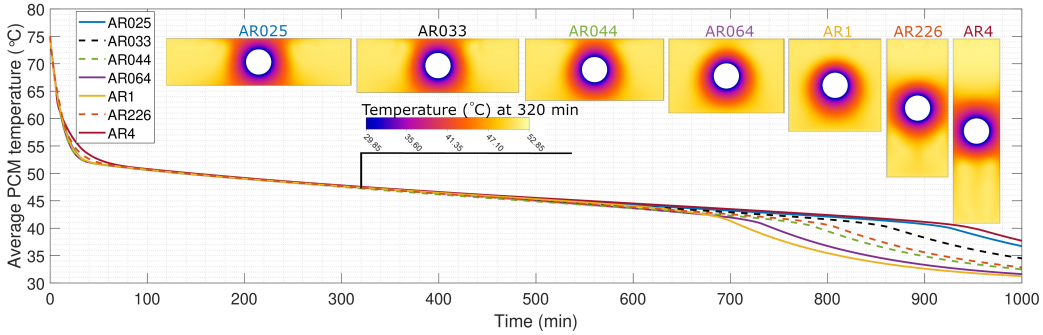

Figure 23. Average PCM temperature over time during solidification for periodic LHTES units with various aspect ratios.

Figures 24 and 25 compare the average heat flux at the the top (a) and bottom (b) edges during the melting and solidification process, respectively. At the beginning of the melting process, configurations with a low aspect ratio are characterised by a rapid increase in absolute heat flux at the top and bottom edges of the shell. This indicates that the liquid PCM reaches the shell edge relatively quickly and begins to heat the unit above. In the case of large aspect ratios (AR226 and AR4), the contact between the liquid PCM and the top wall occurs later, but the absolute heat flux values stabilise around 800 W/m^2, unlike the 500–600 W/m^2 range observed in other configurations (AR025, AR033, AR044, AR064, and AR1). This difference is due to the higher PCM temperature at the upper part of the unit compared to flatter configurations, leading to a greater temperature difference between the top and bottom shell edges. After the melting process is complete, a rapid decrease in heat flux is visible, which is the result of the rapidly decreasing temperature difference between the top and bottom surfaces of the unit. At the beginning of the solidification process, the absolute heat flux at the top and bottom shell edges increases rapidly. The cold liquid PCM moves downward, initiating heat transfer at the top and bottom shell edges due to the temperature difference and the periodic unit structure. The heat flux peak is highest for the AR4 and AR226 cases because, in these configurations, the hot liquid PCM accumulates in the upper part due to the greater distance from the heat source. Consequently, the temperature difference between the top and bottom of the unit is the highest. The downward convection currents gradually weaken, and the absolute heat flux decreases and stabilises. The temperature distribution becomes homogeneous, and conduction dominates.

In Figures 26 and 27, we compare the specific enthalpy change over time during the melting and solidification process, respectively. The specific enthalpy change in the PCM domain is calculated as average values over the domain, and the maximum enthalpy during the melting and solidification processes is equal to 294.5 kJ/kg and 301.5 kJ/kg (Equation (19)), respectively.

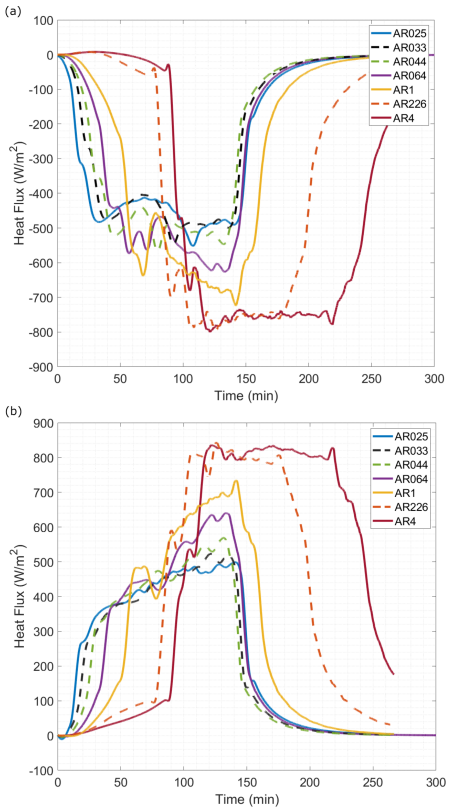

Figure 24. Heat flux average values for the top (**a**) and bottom (**b**) edges during melting.

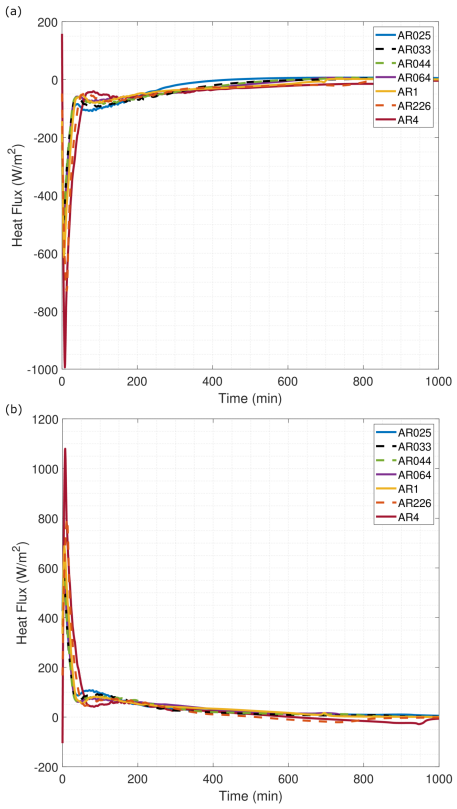

Figure 25. Heat flux average values for the top (**a**) and bottom (**b**) edges during solidification.

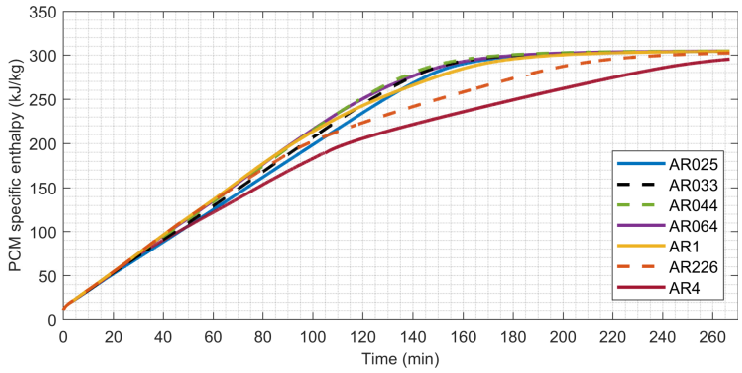

Figure 26. Specific enthalpy over time during melting for periodic LHTES units with various aspect ratios.

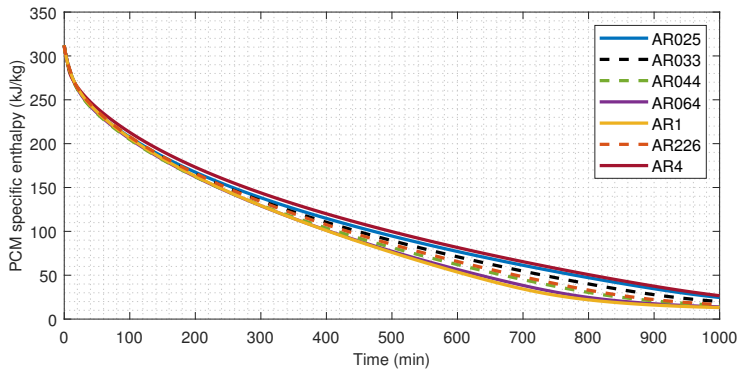

Figure 27. Specific enthalpy over time during solidification for periodic LHTES units with various aspect ratios.

The highest specific enthalpy change during melting, occurring in the shortest time, is achieved in the AR044 case (143 min). All seven cases exhibit a moderate linear increase in specific enthalpy (up to 100 min), indicating that the PCM absorbs heat and transitions from solid to liquid, regardless of the shell aspect ratios. This behaviour is characteristic of the initial phase of the melting process. The specific enthalpy increases most slowly (after 100 min) in the AR226 and AR4 cases. For configurations with an aspect ratio smaller than one, the enthalpy changes are similar, and the differences are small. The maximum time differences to reach the same enthalpy level do not exceed 17 min. These observations correlate with changes in the average PCM temperature and the liquid fraction over time. The highest specific enthalpy change during solidification, occurring in the shortest time, is achieved in the AR1 case (699 min). All seven cases (AR1a, AR1b, and AR1c) show the same enthalpy decrease up to the 100th min. The clear differences in enthalpy level visible after this time are also correlated with the average PCM temperature and liquid fraction over time. The maximum time difference to reach the same enthalpy level is about 200 min, and in the context of the discharging stage, it is an important difference.

5. Conclusions

In this research, we propose a horizontal periodic shell-and-tube structure as an efficient latent heat thermal energy storage unit. We compare this approach to a single shell-and-tube unit with either an insulated adiabatic shell or highly conductive shell. Additionally, we examine the impact of the rectangular shell aspect ratio on the melting and solidification times, spatial and temporal liquid fractions, PCM temperature distributions, and heat fluxes. We employ an enthalpy–porosity numerical model, along with the Boussinesq approximation to address the heat transfer challenges encountered during melting and solidification. A summary of the main outcomes of the research is presented below:

- The horizontal shell-and-tube, used as a periodic structure is an efficient LHTES unit with short melting and solidification times.
- In the non-periodic case with a highly conductive shell (AR1b), the melting time increases by 123.8% and the solidification time by 8.2%, compared to the periodic unit (AR1c).
- In the non-periodic case with neglected conduction in the shell (AR1a), the melting time increases by 213.8% and the solidification time by 21%, compared to the periodic unit (AR1c).
- For shell materials with good thermal conductivity, accounting for conduction in the shell is crucial, resulting in relative differences in melting and solidification times of 26.7% and 10.6%, respectively.
- In the periodic horizontal shell-and-tube structure, additional convection heat transfer occurs in the lower part of the unit.
- The solidification process is more uniform in the periodic unit AR1c than in non-periodic AR1a and AR1b.
- The shortest melting time (143 min) is recorded for the case with a periodic structure and shell aspect ratio equal to 0.44.
- The shortest solidification time (699 min) is recorded for the case with a periodic structure and a shell aspect ratio equal to 1.
- In the initial stage of the phase change phenomena, as the liquid fraction approaches either 25% for melting or 75% for solidification, the aspect ratio of the shell has no effect on the duration of these processes.

We suggest expanding the investigation by modelling various tube placements and multi-tube arrangements within polygonal multi-module LHTES systems. Furthermore, multi-objective optimisation analysis that examines the economic aspects, feasibility, and phase change cycles is crucial for TES projects regarding construction, total PCM volume, and maintaining shape stability.

Author Contributions: Conceptualisation, J.W.; investigation, J.W. and K.S.; methodology, J.W.; supervision, J.W.; validation, K.S.; writing—original draft, J.W. and K.S. All authors have read and agreed to the published version of the manuscript.

Funding: This research was supported in part by Poland national subvention, Poland no. 16.16.130.942. and we gratefully acknowledge Polish high-performance computing infrastructure PLGrid (HPC Center: ACK Cyfronet AGH) for providing computer facilities and support within computational grant no. PLG/2024/017349.

Data Availability Statement: The original contributions presented in the study are included in the article, further inquiries can be directed to the corresponding authors.

Conflicts of Interest: The authors declare no conflicts of interest.

Abbreviations

The following abbreviations are used in this manuscript:

AR	Aspect ratio
DSC	Differential scanning calorimetry
HTF	Heat transfer fluid
LF	Liquid fraction
LHTES	Latent heat thermal energy storage
PCM	Phase-change material
RES	Renewable energy source
TES	Thermal energy storage
Nomenclature	
A_{mush}	Mushy zone
b	Heat transfer coefficient, $W/(m^2 \cdot K)$
c_p	Specific heat capacity, $J/(kg \cdot K)$
g	Gravitational acceleration, m/s^2
h	Specific enthalpy, J/kg
k	Thermal conductivity, $W/(m \cdot K)$
l	Latent heat, J/kg
n	Normal vector
Nu	Nusselt number
p	Pressure, Pa
Pr	Prandtl number
r	Radius, m
R	Thermal resistance, $(m \cdot K)/W$
Ra	Rayleigh number
Re	Reynolds number
S	Momentum source term
Ste	Stefan number
T	Temperature, °C
t	Time, s
v	Fluid flow velocity, m/s
Greek symbols	
α	Liquid fraction
β	Expansion coefficient, 1/K
μ	Dynamic viscosity, $Pa \cdot s$
ρ	Density, kg/m^3
Subscripts	
avg	Average
htf	Fluid, heat transfer fluid (HTF)
i	Particular control volume
ref	Reference
si	Shell inner
t	Tube domain
ti	Tube inner
to	Tube outer

References

1. Nasimi, S.; Fakhroleslam, M.; Zarei, G.; Sadrameli, S.M. Passive energy-efficiency optimization in greenhouses using phase change materials; a comprehensive review. *J. Energy Storage* **2024**, *90*, 111762. [CrossRef]
2. Jayathunga, D.; Karunathilake, H.; Narayana, M.; Witharana, S. Phase change material (PCM) candidates for latent heat thermal energy storage (LHTES) in concentrated solar power (CSP) based thermal applications -A review. *Renew. Sustain. Energy Rev.* **2024**, *189*, 113904. [CrossRef]
3. Huang, X.; Li, F.; Li, Y.; Yang, X.; Li, M.J. Solar photothermal utilization of coupled latent heat storage: A numerical and optimization study. *Sol. Energy Mater. Sol. Cells* **2024**, *271*, 112864. [CrossRef]
4. Migla, L.; Bogdanovics, R.; Lebedeva, K. Performance Improvement of a Solar-Assisted Absorption Cooling System Integrated with Latent Heat Thermal Energy Storage. *Energies* **2023**, *16*, 5307. [CrossRef]
5. Bianco, N.; Fragnito, A.; Iasiello, M.; Mauro, G.M. Multiscale analysis of a seasonal latent thermal energy storage with solar collectors for a single-family building. *Therm. Sci. Eng. Prog.* **2024**, *50*, 102538. [CrossRef]
6. Lazaar, M.; Bouadila, S.; Kooli, S.; Farhat, A. Conditioning of the tunnel greenhouse in the north of Tunisia using a calcium chloride hexahydrate integrated in polypropylene heat exchanger. *Appl. Therm. Eng.* **2014**, *68*, 62–68. [CrossRef]
7. Shan, L.; Martin, A.; Chiu, J.N. Techno-economic analysis of latent heat thermal energy storage integrated heat pump for indoor heating. *Energy* **2024**, *298*, 131291. [CrossRef]
8. Zhai, X.; Lu, S.; He, Z.; Wu, W.; Zhang, H.; Feng, W. Analysis of geo-temperature recovery performance under load redistribution operating strategy of GSHP coupled LHTES device system. *Energy Convers. Manag.* **2024**, *308*, 118402. [CrossRef]
9. Huang, Y.; Deng, Z.; Chen, Y.; Zhang, C. Performance investigation of a biomimetic latent heat thermal energy storage device for waste heat recovery in data centers. *Appl. Energy* **2023**, *335*, 120745. [CrossRef]
10. Hyun, S.W.; Kim, S.; Jeong, H.; Ko, H.S.; Shin, D.H. Development of snow removal system using embedded pipes inside road with solar thermal energy collector and packed bed latent heat thermal energy storage. *J. Energy Storage* **2024**, *83*, 110737. [CrossRef]
11. Jouhara, H.; Żabnieńska Góra, A.; Khordehgah, N.; Ahmad, D.; Lipinski, T. Latent thermal energy storage technologies and applications: A review. *Int. J. Thermofluids* **2020**, *5–6*, 100039. [CrossRef]
12. Punniakodi, B.M.S.; Senthil, R. A review on container geometry and orientations of phase change materials for solar thermal systems. *J. Energy Storage* **2021**, *36*, 102452. [CrossRef]
13. Xie, S.; Wu, W. Effect of aspect ratio on PCM melting behavior in a square cavity. *Int. Commun. Heat Mass Transf.* **2023**, *143*, 106708. [CrossRef]
14. Wan, Y.; Huang, Z.; Soh, A.; Jon Chua, K. On the performance study of a hybrid indirect evaporative cooling and latent-heat thermal energy storage system under commercial operating conditions. *Appl. Therm. Eng.* **2023**, *221*, 119902. [CrossRef]
15. Surya, A.; Prakash, R.; Nallusamy, N. Heat transfer enhancement and performance study on latent heat thermal energy storage system using different configurations of spherical PCM balls. *J. Energy Storage* **2023**, *72*, 108643. [CrossRef]
16. ELSihy, E.S.; Cai, C.; Li, Z.; Du, X.; Wang, Z. Performance investigation on the cascaded packed bed thermal energy storage system with encapsulated nano-enhanced phase change materials for high-temperature applications. *Energy* **2024**, *293*, 130554. [CrossRef]
17. Said, M.A.; Hosseinzadeh, K.; Kaplan, S.; Rahbari, A.; Tiji, M.E.; Mahdi, J.M.; Cairns, A.; Talebizadehsardari, P. Accelerated charging dynamics in shell-and-multi-tube latent heat storage systems for building applications. *J. Energy Storage* **2024**, *81*, 110286. [CrossRef]
18. Ait Laasri, I.; Charai, M.; Mghazli, M.O.; Outzourhit, A. Energy performance assessment of a novel enhanced solar thermal system with topology optimized latent heat thermal energy storage unit for domestic water heating. *Renew. Energy* **2024**, *224*, 120189. [CrossRef]
19. Fornarelli, F.; Dambrosio, L.; Camporeale, S.M.; Terlizzi, L. Novel Multi-Objective Optimal Design of a Shell-and-Tube Latent Heat Thermal Energy Storage Device. *Energies* **2023**, *16*, 1882. [CrossRef]
20. Sheikh, M.I.A.R.; Ahammed, M.E.; Gumtapure, V. Thermal behavior of composite phase change material of polyethylene in a shell and coil-based thermal energy storage: Numerical analysis. *J. Energy Storage* **2023**, *74*, 109438. [CrossRef]
21. Zhao, Y.; Mao, Q. Experimental and numerical analysis of unsteady state conditions on thermal storage performance of a conical spiral shell-tube energy storage system. *J. Energy Storage* **2024**, *88*, 111579. [CrossRef]
22. Punniakodi, B.M.S.; Senthil, R. Enhanced heat transfer in a phase change energy storage with helical tubes. *J. Energy Storage* **2023**, *58*, 106352. [CrossRef]
23. Al-Shuwaili, H.; Kakhki, M.S.; Al-Aridhee, S.; Ghorbani, A.; Entezari, S.; Sardarabadi, M. Performance enhancement of triplex-tube heat storage unit using branched fins during solidification and melting processes: A 2D numerical parametric investigation. *Therm. Sci. Eng. Prog.* **2023**, *38*, 101653. [CrossRef]
24. Wołoszyn, J.; Szopa, K.; Czerwiński, G. Enhanced heat transfer in a PCM shell-and-tube thermal energy storage system. *Appl. Therm. Eng.* **2021**, *196*, 117332. [CrossRef]
25. Mousavi Ajarostaghi, S.S.; Amirsoleymani, A.; Arıcı, M.; Dolati, A.; Amiri, L. Thermal energy storage with PCMs: A comprehensive study of horizontal shell and multi-tube systems with finned design. *J. Energy Storage* **2023**, *72*, 108762. [CrossRef]
26. Rogowski, M.; Andrzejczyk, R. Recent advances of selected passive heat transfer intensification methods for phase change material-based latent heat energy storage units: A review. *Int. Commun. Heat Mass Transf.* **2023**, *144*, 106795. [CrossRef]

27. Czerwiński, G.; Wołoszyn, J. Partitions influence on rectangular latent heat thermal energy storage unit performance during melting and solidification. *Int. Commun. Heat Mass Transf.* **2024**, *159*, 108047. [CrossRef]
28. Low, Z.H.; Qin, Z.; Duan, F. A review of fin application for latent heat thermal energy storage enhancement. *J. Energy Storage* **2024**, *85*, 111157. [CrossRef]
29. Kaboré, A.; Simo Tala, J.V.; Younsi, Z.; Bougeard, D. Natural convection and field synergy principle analysis of the influence of fins redistribution on the performance of a latent heat storage unit in a successive charge and discharge. *J. Energy Storage* **2024**, *89*, 111855. [CrossRef]
30. Hosseini, A.; Banakar, A.; Gorjian, S.; Jafari, A. Experimental and numerical investigation of the melting behavior of a phase change material in a horizontal latent heat accumulator with longitudinal and annular fins. *J. Energy Storage* **2024**, *82*, 110563. [CrossRef]
31. Ao, C.; Yan, S.; Zhao, X.; Zhang, N.; Wu, Y. Enhanced heat transfer in a latent heat thermal energy storage unit using a longitudinal fin with different structural parameters. *Therm. Sci. Eng. Prog.* **2023**, *43*, 101975. [CrossRef]
32. Li, H.; Hu, C.; Tang, D.; Rao, Z. Improving heat storage performance of shell-and-tube unit by using structural-optimized spiral fins. *J. Energy Storage* **2024**, *79*, 110212. [CrossRef]
33. Li, J.; Abdulghani, Z.R.; Alghamdi, M.N.; Sharma, K.; Niyas, H.; Moria, H.; Arsalanloo, A. Effect of twisted fins on the melting performance of PCM in a latent heat thermal energy storage system in vertical and horizontal orientations: Energy and exergy analysis. *Appl. Therm. Eng.* **2023**, *219*, 119489. [CrossRef]
34. Guedri, K.; Singh, P.; Riaz, F.; Inayat, A.; Shah, N.A.; Fadhl, B.M.; Makhdoum, B.M.; Arsalanloo, A. Solidification acceleration of phase change material in a horizontal latent heat thermal energy storage system by using spiral fins. *Case Stud. Therm. Eng.* **2023**, *48*, 103157. [CrossRef]
35. Sarani, I.; Payan, S.; Nada, S.; Payan, A. Numerical investigation of an innovative discontinuous distribution of fins for solidification rate enhancement in PCM with and without nanoparticles. *Appl. Therm. Eng.* **2020**, *176*, 115017. [CrossRef]
36. Luo, M.; Zhang, Y.; Niu, Y.; Lu, B.; Wang, Z.; Zhang, J.; Wang, K.; Zhu, J. Experimental and numerical investigations on the thermal performance enhancement of a latent heat thermal energy storage unit with several novel snowflake fins. *Renew. Energy* **2023**, *217*, 119158. [CrossRef]
37. Qasem, N.A.; Abderrahmane, A.; Belazreg, A.; Younis, O.; Homod, R.Z.; Oreijah, M.; Guedri, K. Influence of tree-shaped fins to enhance thermal storage units. *Int. Commun. Heat Mass Transf.* **2024**, *151*, 107220. [CrossRef]
38. Czerwiński, G.; Wołoszyn, J. Influence of the Longitudinal and Tree-Shaped Fin Parameters on the Shell-and-Tube LHTES Energy Efficiency. *Energies* **2022**, *16*, 268. [CrossRef]
39. Triki, R.; Chtourou, S.; Baccar, M. Heat transfer enhancement of phase change materials PCMs using innovative fractal H-shaped fin configurations. *J. Energy Storage* **2023**, *73*, 109020. [CrossRef]
40. Wang, Y.; Zadeh, P.G.; Duong, X.Q.; Chung, J.D. Optimizing fin design for enhanced melting performance in latent heat thermal energy storage systems. *J. Energy Storage* **2023**, *73*, 109108. [CrossRef]
41. Wołoszyn, J.; Wyciszkiewicz, G. Modelowanie przemiany fazowej w potrójnym systemie rurowym wzmocnionym żebrami. *Przemysł Chem.* **2021**, *1*, 101–104. [CrossRef]
42. Sundriyal, A.; Verma, P.; Varshney, L. Numerical study of the melting rate enhancement of nano phase change material in a modified shell and tube heat exchanger. *J. Energy Storage* **2024**, *84*, 110859. [CrossRef]
43. Li, Z.R.; Zhang, Z.K.; Wang, X.R.; Ni, S.S.; Fan, L.W. Synergistic enhancement strategy on the heat charging process of a shell-and-tube thermal storage device based on close-contact melting mechanism and nano-enhanced phase change material. *J. Energy Storage* **2023**, *72*, 108529. [CrossRef]
44. Buonomo, B.; Golia, M.R.; Manca, O.; Nardini, S.; Plomitallo, R.E. External heat losses effect on shell and tube latent heat thermal energy storages partially filled with metal foam. *J. Energy Storage* **2024**, *85*, 111096. [CrossRef]
45. Zhang, Z.; Zhu, Z. Thermodynamic performance improvement of the horizontal shell-and-tube latent heat thermal storage unit by splitter plates and upper-and-lower cascade PCMs. *J. Energy Storage* **2024**, *83*, 110802. [CrossRef]
46. Yang, X.; Li, Y.; Ma, Y.; Cui, J.; Xie, J. Optimization of thermal storage performance of cascaded multi-PCMs and carbon foam energy storage system based on GPR-PSO algorithm. *J. Energy Storage* **2024**, *83*, 110626. [CrossRef]
47. Sayoud, N.; Laouer, A.; Brihi, N.; Teggar, M.; Arıcı, M. Melting process enhancement in double pipe storage with multiple latent heat storage materials and oriented fins. *J. Energy Storage* **2024**, *85*, 111095. [CrossRef]
48. Zhou, S.; Dai, H.; Gao, M.; He, S.; Niu, P.; Shi, Y.; Qi, J.; Sun, F. Influence of inner tube shapes on the charging and discharging performance for the latent heat thermal storage exchangers. *Int. Commun. Heat Mass Transf.* **2024**, *154*, 107466. [CrossRef]
49. Alnakeeb, M.A.; Galal, W.M.; Youssef, M.E.; Sorour, M.M. Melting characteristics of concentric and eccentric inner elliptic tube in double tube latent heat energy storage unit. *Alex. Eng. J.* **2023**, *73*, 443–460. [CrossRef]
50. Peng, L.; Wu, H.; Cao, W.; Mao, Q. Exergy Analysis of a Shell and Tube Energy Storage Unit with Different Inclination Angles. *Energies* **2023**, *16*, 4297. [CrossRef]
51. Togun, H.; Sultan, H.S.; Mohammed, H.I.; Sadeq, A.M.; Biswas, N.; Hasan, H.A.; Homod, R.Z.; Abdulkadhim, A.H.; Yaseen, Z.M.; Talebizadehsardari, P. A critical review on phase change materials (PCM) based heat exchanger: Different hybrid techniques for the enhancement. *J. Energy Storage* **2024**, *79*, 109840. [CrossRef]

52. Saini, P.; Dhar, A.; Powar, S.; Doddamani, M. Cesaro fins parametric optimization for enhancement in the solidification performance of a latent heat storage system with combined fins, foam, and nanoparticle. *Energy Rep.* **2023**, *9*, 5670–5687. [CrossRef]
53. Shank, K.; Tiari, S. A Review on Active Heat Transfer Enhancement Techniques within Latent Heat Thermal Energy Storage Systems. *Energies* **2023**, *16*, 4165. [CrossRef]
54. Kumar, A.; Verma, P.; Varshney, L. An experimental and numerical study on phase change material melting rate enhancement for a horizontal semi-circular shell and tube thermal energy storage system. *J. Energy Storage* **2022**, *45*, 103734. [CrossRef]
55. Faghani, M.; Hosseini, M.; Bahrampoury, R. Numerical simulation of melting between two elliptical cylinders. *Alex. Eng. J.* **2018**, *57*, 577–586. [CrossRef]
56. Rabienataj Darzi, A.A.; Jourabian, M.; Farhadi, M. Melting and solidification of PCM enhanced by radial conductive fins and nanoparticles in cylindrical annulus. *Energy Convers. Manag.* **2016**, *118*, 253–263. [CrossRef]
57. Khillarkar, D.; Gong, Z.; Mujumdar, A. Melting of a phase change material in concentric horizontal annuli of arbitrary cross-section. *Appl. Therm. Eng.* **2000**, *20*, 893–912. [CrossRef]
58. Mao, Q.; Chen, K.; Li, T. Heat transfer performance of a phase-change material in a rectangular shell-tube energy storage tank. *Appl. Therm. Eng.* **2022**, *215*, 118937. [CrossRef]
59. Li, J.; Huang, Y.; Zhang, C.; Liu, X. Numerical study on the solidification performance of a latent heat storage unit with Koch-fractal fin. *Fractals* **2019**, *27*, 1950108. [CrossRef]
60. Alizadeh, M.; Haq, R.; Hamid, M.; Nguyen, V.; Truong, T.; Ganji, D.; Tian, Z. An analysis of latent heat thermal energy storage in a hexagonal triplex-tube unit with curve shape fin and CNTs. *Case Stud. Therm. Eng.* **2022**, *36*, 102241. [CrossRef]
61. Maneengam, A.; Ahmed, S.E.; Saeed, A.M.; Abderrahmane, A.; Younis, O.; Guedri, K.; Alhazmi, M.; Weera, W. Numerical Study of Heat Transfer Enhancement within Confined Shell and Tube Latent Heat Thermal Storage Microsystem Using Hexagonal PCMs. *Micromachines* **2022**, *13*, 1062. [CrossRef]
62. Shahsavar, A.; Al-Rashed, A.A.; Entezari, S.; Sardari, P.T. Melting and solidification characteristics of a double-pipe latent heat storage system with sinusoidal wavy channels embedded in a porous medium. *Energy* **2019**, *171*, 751–769. [CrossRef]
63. Shahsavar, A.; Shaham, A.; Yıldız, Ç.; Arıcı, M. Entropy generation characteristics of phase change material in a variable wavy walled triplex tube latent heat storage unit for battery thermal management system. *J. Energy Storage* **2022**, *51*, 104374. [CrossRef]
64. Alizadeh, M.; Nabizadeh, A.; Fazlollahtabar, A.; Ganji, D. An optimization study of solidification procedure in a wavy- wall storage unit considering the impacts of NEPCM and curved fin. *Int. Commun. Heat Mass Transf.* **2021**, *124*, 105249. [CrossRef]
65. Wołoszyn, J.; Szopa, K. A combined heat transfer enhancement technique for shell-and-tube latent heat thermal energy storage. *Renew. Energy* **2023**, *202*, 1342–1356. [CrossRef]
66. Qaiser, R.; Khan, M.M.; Khan, L.A.; Irfan, M. Melting performance enhancement of PCM based thermal energy storage system using multiple tubes and modified shell designs. *J. Energy Storage* **2021**, *33*, 102161. [CrossRef]
67. Hekmat, M.H.; Haghani, M.H.K.; Izadpanah, E.; Sadeghi, H. The influence of energy storage container geometry on the melting and solidification of PCM. *Int. Commun. Heat Mass Transf.* **2022**, *137*, 106237. [CrossRef]
68. Wołoszyn, J.; Szopa, K. Shell Shape Influence on Latent Heat Thermal Energy Storage Performance during Melting and Solidification. *Energies* **2023**, *16*, 7822. [CrossRef]
69. Chen, D.; Riaz, A.; Aute, V.C.; Radermacher, R. Comprehensive performance analysis and structural improvement of latent heat thermal energy storage (LHTES) unit using a novel parallel enthalpy-based lattice Boltzmann model. *J. Energy Storage* **2023**, *73*, 108902. [CrossRef]
70. Modi, N.; Wang, X.; Negnevitsky, M. Numerical investigation into selecting the most suitable shell-to-tube diameter ratio for horizontal latent heat thermal energy storage. *Energy Sustain. Dev.* **2023**, *73*, 188–204. [CrossRef]
71. Kalapala, L.; Devanuri, J.K. Influence of operational and design parameters on the performance of a PCM based heat exchanger for thermal energy storage – A review. *J. Energy Storage* **2018**, *20*, 497–519. [CrossRef]
72. Parsa, N.; Kamkari, B.; Abolghasemi, H. Experimental study on the influence of shell geometry and tube eccentricity on phase change material melting in shell and tube heat exchangers. *Int. J. Heat Mass Transf.* **2024**, *227*, 125571. [CrossRef]
73. Su, Q.; Xiong, X.; Zhu, C.; Li, J.; Duan, J.; Jin, W.; Wang, Y. Experimental and numerical investigation on the melting behavior of paraffin in a shell and tube latent heat storage unit. *Appl. Therm. Eng.* **2024**, *236*, 121374. [CrossRef]
74. Chen, L.; Fan, A. Effects of shell modifications and operational parameters on melting uniformity of a vertical multi-section shell-and-tube latent heat thermal energy storage unit. *J. Energy Storage* **2022**, *55*, 105593. [CrossRef]
75. Ding, P.; Liu, Z. Numerical investigation of natural convection enhancement in latent heat energy storage units with punched-fin and slit-fin. *Int. J. Therm. Sci.* **2021**, *163*, 106834. [CrossRef]
76. Bergman, T.L.; Lavine, A.S.; Incropera, F.P.; Dewitt, D.P. *Fundamentals of Heat and Mass Transfer*, 8th ed.; Wiley: Hoboken, NJ, USA, 2017; p. 1046.
77. ANSYS. *ANSYS Fluent Theory Guide 2020*; ANSYS, Inc.: Canonsburg, PA, USA, 2020.
78. Voller, V.R.; Prakash, C. A fixed grid numerical modelling methodology for convection-diffusion mushy region phase-change problems. *Int. J. Heat Mass Transf.* **1987**, *30*, 1709–1719. [CrossRef]
79. Anderson, D.; Tannehill, J.C.; Pletcher, R.H. *Computational Fluid Mechanics and Heat Transfer*, 3rd ed.; CRC Press: Boca Raton, FL, USA, 2016; pp. 1–740.

80. Kousha, N.; Hosseini, M.J.; Aligoodarz, M.R.; Pakrouh, R.; Bahrampoury, R. Effect of inclination angle on the performance of a shell and tube heat storage unit – An experimental study. *Appl. Therm. Eng.* **2017**, *112*, 1497–1509. [CrossRef]
81. Tiari, S.; Qiu, S.; Mahdavi, M. Numerical study of finned heat pipe-assisted thermal energy storage system with high temperature phase change material. *Energy Convers. Manag.* **2015**, *89*, 833–842. [CrossRef]
82. Karami, R.; Kamkari, B. Investigation of the effect of inclination angle on the melting enhancement of phase change material in finned latent heat thermal storage units. *Appl. Therm. Eng.* **2019**, *146*, 45–60. [CrossRef]
83. Sardari, P.T.; Babaei-Mahani, R.; Giddings, D.; Yasseri, S.; Moghimi, M.A.; Bahai, H. Energy recovery from domestic radiators using a compact composite metal Foam/PCM latent heat storage. *J. Clean. Prod.* **2020**, *257*, 120504. [CrossRef]
84. Shmueli, H.; Ziskind, G.; Letan, R. Melting in a vertical cylindrical tube: Numerical investigation and comparison with experiments. *Int. J. Heat Mass Transf.* **2010**, *53*, 4082–4091. [CrossRef]
85. Fadl, M.; Eames, P.C. Numerical investigation of the influence of mushy zone parameter Amush on heat transfer characteristics in vertically and horizontally oriented thermal energy storage systems. *Appl. Therm. Eng.* **2019**, *151*, 90–99. [CrossRef]
86. Ye, W.B.; Arıcı, M. Exploring mushy zone constant in enthalpy-porosity methodology for accurate modeling convection-diffusion solid-liquid phase change of calcium chloride hexahydrate. *Int. Commun. Heat Mass Transf.* **2024**, *152*, 107294. [CrossRef]
87. Sutheesh, P.; Jose, J.; Hotta, T.K.; Rohinikumar, B. Numerical investigations on thermal performance of PCM-based lithium-ion battery thermal management system equipped with advanced honeycomb structures. *Int. Commun. Heat Mass Transf.* **2024**, *158*, 107937. [CrossRef]